# Dynamical Response of Horizontal Temperature Fields in the Mid-latitude Thermocline to the Decadal Variation of Wind Stress Curl

Hirohiko Nakamura

# 風系の数十年変動に起因する中緯度温度躍層における水平温度場の力学的応答

中村 啓彦

# Dynamical Response of Horizontal Temperature Fields in the Mid-latitude Thermocline to the Decadal Variation of Wind Stress Curl

Thesis for a Doctorate

**Hirohiko Nakamura**

*Division of Geophysics, Graduate School of Science,*

*Hokkaido University*

July 31, 1995

# Contents

# Abstract

A major objective of this paper is to propose the mechanism that generates the variability in thermohaline structures, which was actually observed at intermediate depths of the North Atlantic subtropical-subpolar gyres, with interdecadal time scales. The observed variability is first compared with the climatological mean thermohaline structures and related to the observed variability in the wind stress curl over the North Atlantic. This data analysis yields two hypotheses: 1) a primary cause of the observed variability in thermohaline structures was the weakened wind stress curl, and 2) the thermohaline variability caused by a uniform change in the wind stress curl was different between the western and eastern portions in both subtropical and subpolar gyres.

In order to test these hypotheses, a four-level model, which is driven by wind stresses and surface buoyancy flux, is constructed with thermohaline structures represented by a temperature field. The model is used to examine responses of the subtropical-subpolar thermohaline field to a sudden and uniform change in wind stress curl. The model demonstrates that the uniformly weakened wind stress curl generates the thermohaline change with different tendencies between the western and eastern domains in both subtropical and subpolar gyres, similar to the observed pattern.

The thermohaline change with different tendencies between the western and eastern domains is not related to a previous linear theory, which is associated with the local Ekman pumping and the long baroclinic Rossby wave. In this study, the responses of the subtropical-subpolar thermohaline field are examined on the basis of a non-linear theory, which is associated with nonlinear advection in addition to above two mechanisms. The model solutions are analyzed using an analytical method: i.e., the characteristic curves associated with both a linear wave propagation and nonlinear advection effects.

The mechanism which generates the thermohaline change with different tendencies between the western and eastern domains is summarized as follows: the 1st baroclinic velocity field is weakened by the vertical shift of the temperature field in both subtropical and subpolar gyres. This process almost corresponds to the linear response. The weakened

1st baroclinic velocity field forms temperature anomalies in the thermocline, which have different tendencies between the western and eastern domains in both subtropical and subpolar gyres. The formation areas of temperature anomalies are related to the mean horizontal temperature structures, which are maintained by the wind stresses and surface buoyancy flux. The propagation of temperature anomalies along the characteristics generates the horizontal shift of temperature field.

# 1 Introduction

The oceans have the large heat capacity as compared to the atmosphere, and also the ability to transport heat over large distances. Thus, the oceans are likely to play a key role in setting the time scale for the interdecadal climate variability (O'Brien, 1992). In the mid-latitude, the large-scale oceanic circulations transport heat poleward at intermediate depths, and the heat transported poleward is transferred to the atmosphere by air-sea interactions. The cumulative effect of air-sea interactions in the mid-latitude is important in the zonally asymmetric part of the atmospheric circulation, and hence horizontal distribution of climate. Kushnir (1994) suggested that the interdecadal variability of sea surface temperature in the mid-latitude North Atlantic might be governed by a basin-scale dynamical interaction between the large-scale oceanic circulation and atmosphere. The large-scale oceanic circulation is mainly related to the thermohaline structures at intermediate depths. Thus, the interdecadal variability in thermohaline structures at intermediate depths might be fundamental as the oceanic process which drives the interdecadal climate variability.

The interdecadal variability in the thermohaline structures was actually observed at intermediate depths of the North Atlantic. The time series of temperature at the Panulirus Station (located near Bermuda) in the subtropical North Atlantic showed that temperature decreased with a maximum value of 1°C in the 0 to 1200m depth range throughout 1960's(Talley and Raymer, 1982; Roemmich, 1985). Levitus (1989) described basin-scale changes in the thermohaline structures at intermediate depths of the North Atlantic during the 1955-1959 and 1970-1974 periods. A major feature in the basin-scale changes was that the thermohaline change had different tendencies between the western and eastern portions in both subtropical and subpolar gyres (see Fig.1a and Fig.1b). Furthermore, Greatbatch et al. (1991) and Greatbatch and Xu (1993) discussed changes in the transport of volume and heat between the 1955-1959 and 1970-1974 periods, based on the diagnostic calculation using density data from Levitus (1989). They showed that the

Gulf Stream was considerably weaker in the 1970-1974 period than in the 1955-1959 period. However, the previous studies have not yet clarified the mechanism which generated the observed variability in the thermohaline structures.

A major objective of this paper is to propose the mechanism which generated the observed variability in the thermohaline structures at intermediate depths of the North Atlantic. A main feature of the observed variability is that the thermohaline change had different tendencies between the western and eastern domains in both the subtropical and subpolar gyres. We particularly propose the mechanism which formed the horizontal pattern of the observed thermohaline change.

Although the previous studies did not establish the mechanism which generated the observed thermohaline variability, possible mechanisms were suggested. The temporal variability of the wind stress curl could change the thermohaline structure at intermediate depths because of the vertical displacement of the thermocline. This process was responsible for the observed shoaling of the density surface (hence, cooling/freshening) at intermediate depths in the western subtropical gyre throughout 1960's (Talley and Raymer, 1982; Roemmich, 1985; Levitus, 1989). In addition, the change in convection could play a major role in modifying the thermohaline structure at the upper few hundred meters of the subtropical ocean through the isopycnal flow. This process was responsible for a decrease in potential vorticity of the Subtropical Mode Water throughout 1960's (Tally and Raymer, 1982; Levitus, 1989), although the cause which changed convection was not discussed in these papers. Furthermore, Levitus (1989) suggested that the change in the thermohaline structure of the subpolar gyre was affected by "Great Salinity Anomaly"; the cooling and freshening began at the upper ocean (0-200m) of the Northern North Atlantic in the mid-1960's, and then the cold and flesh water propagated around the subpolar gyre during the 1960's and 1970's (e.g., Dickson et al., 1988).

Several mechanisms might cause the observed thermohaline variability. In this paper, the observed thermohaline variability is examined through the response to the observed variability in the wind stress curl over the North Atlantic. In addition, the observed

horizontal pattern of thermohaline change with different tendencies between the western and eastern portions, is examined through the non-linear response of the ocean to the wind variation. A simple level model is used to examine the mechanism which generated the observed thermohaline variability.

The problem studied by using the simple numerical model is to clarify the dynamical response of the horizontal temperature fields in the mid-latitude thermocline to the decadal variation of the wind stress curl. This problem with respect to the time-dependent thermocline structure on the mid-latitude $\beta$ plane ocean, has been theoretically studied. Most of the previous studies focused on the local Ekman pumping and the non-dispersive long baroclinic Rossby waves which were mostly excited at the eastern boundary (e.g., Anderson and Gill, 1975; Anderson and Killworth, 1979). Recently, Liu(1993a, b, 1994) studied the time-dependent thermocline structure in a ventilated thermocline model. His studies emphasized the effect of the ventilation in adding to two mechanisms above. This paper also pays attention to non-linear advection effects on the time-dependent thermocline structure.

Although Liu (1993a, b, 1994) gave us the physical insight on the time-dependent thermocline structure in the interior region of the subtropical gyre, these cannot answer the following questions: 1) what is the variation of the thermocline in the subtropical-subpolar system which includes the western boundary, and 2) what is the variation of the thermocline in the subtropical-subpolar system which is driven by combined wind and buoyancy flux. This paper tries to answer these questions. Thus, the simple numerical model used in this study is represented by the subtropical-subpolar closed system which includes the western boundary, and driven by the wind stress and surface heat flux. Furthermore, we interpret the dynamics of the time-dependent thermocline structure in the model by using an analytical method; i.e., the characteristic curves associated with a linear wave propagation and non-linear advection effects.

This paper is organized as follows: in section 2, the horizontal spatial pattern of the thermohaline change shown by Levitus(1989) is compared with the climatological

mean structure, then the temporal and spatial variation of the wind stress curl over the North Atlantic is examined, finally we summarize observational evidences. In section 3, the numerical model and governing equations are first described, and next the outline of numerical experiments is explained. In section 4, the dynamics of time-dependent horizontal temperature fields in the thermocline are preliminary discussed based on the level model used in this study. In section 5, the results of numerical experiments are presented. First, the model solutions are compared with the observational evidences in the North Atlantic. Second, the steady state solutions are analyzed. Third, the time-dependent solutions are analyzed. In addition, the variation in the meridional circulation is discussed. In section 6, we discuss generally the results of numerical experiments. In section 7, conclusive remarks of this paper are given.

# 2 Observational evidences in the North Atlantic

## 2.1 Spatial pattern of the variation in the temperature and salinity structures

Figures 1a and 1b quoted from Levitus (1989) show the horizontal temperature and salinity structure changes at 500m depth in the North Atlantic during the 1955-1959 and 1970-1974 periods, respectively. Both temperature and salinity changes exhibit a same spatial pattern with different tendencies between the western and eastern portions in subtropical and subpolar gyres. Such feature of the horizontal spatial pattern is described as follows: temperature/salinity decreased in the northwestern subtropical gyre, whereas increased weakly in the southeastern subtropical gyre, on the other hand, temperature/salinity increased in the western subpolar gyre, while decreased in the eastern subpolar gyre in the 1970-1974 period than in the 1955-1959 period.

Figures 1c and 1d show the climatological annual mean horizontal temperature and

salinity structures at 500m depth in the North Atlantic derived from Levitus (1982), respectively. Comparing Fig.1a with Fig.1c, and Fig.1b with Fig.1d, we notice the geographical relationships between the temperature/salinity structure changes and these mean structures. In the subtropical gyre, the western and eastern portions, which are characterized by the different tendencies of temperature/salinity changes, are separated by a dashed curve in Fig.1c and Fig.1d; this curve is characterized by points at which mean isothermal/isohaline contours turn from southward to eastward direction. This feature in the mean temperature/salinity structures is more remarkable at the subsurface (Fig.2), because this is related to the subtropical front. The region where temperature/salinity decreased significantly in the subtropical gyre was confined to the south of the Gulf Stream system. On the other hand, in the subpolar gyre the region where temperature/salinity decreased existed both on and east of the North Atlantic Current; this is identified by mean isothermal/isohaline contours which extend northward with the strong gradient. The region where temperature/salinity increased in the subpolar gyre existed west of the North Atlantic Current.

Above geographical relationships suggest the dynamical interaction between the temperature/salinity structure changes and mean temperature/salinity structures. As shown in Fig.1, the horizontal structure of mean temperature field is similar to that of mean salinity field, and the horizontal spatial pattern of the temperature change was also similar to that of the salinity change. Thus, it is suggested that the salinity change was generated by the same mechanism as temperature one.

The vertical feature of the temperature structure change is shown in Fig.3a. In this figure, the cooling region at the western subtropical gyre is found in the depth range of the 100 to 1300m, and the weakly warming region at the eastern subtropical gyre is also found in the depth range of the 200 to 1300m. The depth range of the 200 to 1300m approximately corresponds to the permanent thermocline (Fig.3b). It is considered that the observed thermohaline change mainly occurred in the permanent thermocline.

## 2.2 Temporal and spatial variability of the wind stress curl

The interdecadal variation of the wind curl (for the alternative of wind stress curl) over the North Atlantic is examined as a primary cause of the observed thermohaline structure change.

For this purpose, we analyze the monthly mean atmospheric pressure on the ground in the Northern hemisphere during 1946-1988 period, which is compiled over 10° squares in the latitude and longitude ranges by Japan Meteorological Research Institute. Our algorithm of the wind curl calculation is described below. The annual mean atmospheric pressure is first derived from the monthly mean one, and then the annual mean wind is calculated by using the thermal wind relation on the spherical coordinates. Finally, the annual mean wind curl is calculated. The annual mean wind curl is arranged in the region north of 30°N, because the atmospheric pressure is not available in the south of 20°N throughout all period analyzed in this paper.

Figure 4a shows the distribution of the climatological annual mean wind curl averaged during 1952-1988 period. The distribution in Fig.4a is consistent with the prescribed wind stress curl (e.g., Hellerman and Rosenstein, 1983). Furthermore, Figure 4b shows the difference of the wind curl between 1955 and 1970; these years are selected as the first ones of two periods when Levitus (1989) compared the thermohaline structures, because the wind field varies the thermohaline structure with the time lag. Figure 4b indicates that the magnitude of the wind curl decreased over the subtropical and subpolar gyres except the portion near the eastern boundaries of both gyres in 1970 comparing with in 1955. Figure 4c shows the temporal variations in the magnitude of the wind curl in both subtropical and subpolar gyres. It is shown that the magnitude of the wind curl in the subtropical gyre decreased in the period between 1952 and 1971, on the other hand, its magnitude in the subpolar gyre increased in the period between 1952 and 1959, and then decreased to 1971. As a result, Figure 4 shows that the magnitude of the wind curl over the subtropical-subpolar North Atlantic decreased throughout 1960's.

## 2.3 Summary of observational evidences

The results discussed in subsections above are briefly summarized as follows:

1) The thermohaline structure change at intermediate depths of the North Atlantic between 1955-1959 and 1970-1974 periods is characterized by the horizontal spatial pattern with the different tendencies between the western and eastern portions in both subtropical and subpolar gyers. The horizontal pattern of the thermohaline change is geographically related to the mean horizontal thermohaline structure at intermediate depths of the subtropical-subpolar gyres.

2) The observed thermohaline structure change mainly occurred in the permanent thermocline.

3) The magnitude of the wind curl (hence, wind stress curl) over the subtropical-subpolar North Atlantic decreased throughout 1960's.

Above observational evidences yield two hypotheses:

1) A primary cause of the observed thermohaline structure change in the subtropical-subpolar gyres was the weakened wind stress curl over the North Atlantic.

2) The thermohaline change due to a uniform change in the wind stress curl was different between the western and eastern portions, through dynamics in the ocean.

The second hypothesis cannot be explained by the traditional linear theory (e.g., Anderson and Gill, 1975) based on the vertical shift of the thermocline, because the uniform change in the wind stress curl causes the unidirectional vertical shift of the thermocline under the linear theory. Thus, we focus on the horizontal shift of the thermocline through non-linear advection effects in adding to its vertical shift. A simple numerical model is used to examine responses of the subtropical-subpolar thermohaline field to the weakened wind stress curl. As for the numerical experiments, it is possible to investigate only temperature variation for simplicity, because it is suggested that the salinity variation was

generated by the same mechanism as temperature one.

# 3 Description of the numerical model

## 3.1 The model and governing equations

The model used in this study is the four-level model, which is relatively coarse to resolve the temperature stratification but it is useful to analyze the numerical results. The four-level geometry in this model is shown in Fig.5a; the uppermost level (50m) corresponds to the Ekman layer, the second (225m) and third level (225m) correspond to the thermocline, and the deepest level (3500m) corresponds to the deep ocean. Our interests are mainly in the horizontal temperature structures in the second and third levels. The two-level representation of the thermocline is employed to resolve the lowest baroclinic component in the thermocline. The horizontal plane (Fig.5b) is a rectangular closed basin, with the meridional distance of 4560km extending approximately from 15°N to 55°N and the zonal distance of 4080km. This basin scale corresponds to the subtropical-subpolar system in the North Atlantic Ocean. A rigid lid and flat bottom are assumed.

Density $\rho$ may change as temperature and salinity varies. Based on observational evidences, salinity contribution to density is neglected. Thus, density $\rho$ is given by temperature $T$ as,

$$\rho = \rho_c[1 - \alpha(T - T_c)] \tag{3.1.1}$$

where $\rho_c$ and $T_c$ are reference scales, and $\alpha = 2.5 \times 10^{-4}$ °C$^{-1}$ is the thermal expansion coefficient.

Three-dimensional Navier-Stokes equations are simplified by the following assumptions. Hydrostatic and Boussinesq approximations are used, and nonlinear advection terms are omitted. As a result, the governing equations are written as

$$\frac{\partial}{\partial t}u - fv = -\frac{1}{\rho_0}\frac{\partial}{\partial x}p + A_{MH}\nabla_H^2 u + A_{MV}\frac{\partial^2}{\partial z^2}u \tag{3.1.2}$$

$$\frac{\partial}{\partial t}v + fu = -\frac{1}{\rho_0}\frac{\partial}{\partial y}p + A_{MH}\nabla_H^2 v + A_{MV}\frac{\partial^2}{\partial z^2}v \tag{3.1.3}$$

$$\frac{\partial}{\partial z}p = -\rho g \tag{3.1.4}$$

$$\frac{\partial}{\partial x}u + \frac{\partial}{\partial y}v + \frac{\partial}{\partial z}w = 0 \tag{3.1.5}$$

$$\frac{\partial}{\partial t}T + \frac{\partial}{\partial x}(uT) + \frac{\partial}{\partial y}(vT) + \frac{\partial}{\partial z}(wT) = A_{DH}\nabla_H^2 T + A_{DV}\frac{\partial^2}{\partial z^2}T + CA(T) \tag{3.1.6}$$

where $\nabla_H^2 = \partial^2/\partial x^2 + \partial^2/\partial y^2$. The zonal, meridional and vertical coordinates are denoted by $x$, $y$ and $z$ respectively, along with the corresponding velocities $u$, $v$ and $w$, $p$ is pressure, $\rho_0 = 1$ gm cm$^{-3}$ is reference density, and $f = f_0 + \beta(y - y_0)$ is Coriolis parameter for the mid-latitude $\beta$ plane (centered at $y_0 = 35°$N), where $f_0 = 8.365 \times 10^{-5}$ s$^{-1}$ and $\beta = 1.873 \times 10^{-13}$ cm$^{-1}$ s$^{-1}$. Furthermore, $A_{MH}$, $A_{DH}$, $A_{MV}$ and $A_{DV}$ are the lateral eddy viscosity, lateral eddy diffusivity, vertical eddy viscosity and vertical eddy diffusivity, respectively. The term $CA$ in the heat equation represents convective adjustment.

There are the boundary conditions to be satisfied. The east and west walls of the basin are impermeable, noslip and insulating boundaries:

$$u = v = \frac{\partial}{\partial x}T = 0 \tag{3.1.7}$$

The southern and northern boundaries are slip, impermeable and insulating boundaries:

$$\frac{\partial}{\partial y}u = v = \frac{\partial}{\partial y}T = 0 \tag{3.1.8}$$

The surface boundary condition for temperature can be written as

$$A_{HV}\frac{\partial}{\partial z}T = \gamma\ (T^*(y) - T_1) \tag{3.1.9}$$

where $\gamma = 30$ cm day$^{-1}$ is the air-sea interaction coefficient, $T^*(y)$ is the reference temperature which is assumed to be zonally uniform (Fig.6), and $T_1$ is temperature of the

uppermost level. The wind stress applied to the uppermost level is zonally uniform, and is only meridionally variable,

$$A_{MV}(u,\ v) = (\tau^x,\ 0)/\rho_0 \tag{3.1.10}$$

The wind stress profile (Fig.6) to obtain a steady state of temperature and velocity is given by a simple sinusoidal expression, but this profile is shifted to the plus direction in order to avoid the coastal upwelling or downwelling at the southern or northern boundary. Thus, we notice that the meridional profile of Ekman pumping is somewhat different from that of previous theoretical studies through the difference in Ekman transport (Fig.7). However, the wind stress profile in this study forms the same barotropic subtropical-subpolar gyres as that in the previous studies.

The method to integrate the model equations is similar to that of Bryan (1969). The horizontal resolution of the model is 120km×120km. This horizontal grid spacing sets about 4 grid points on the western boundary current; for $\beta = 1.873 \times 10^{-13}$ cm$^{-1}$ s$^{-1}$ and $A_{MH} = 5 \times 10^8$ cm$^2$ s$^{-1}$, the Munk scale is $\sqrt[3]{A_{MH}/\beta}$ ~140km. The model parameters are summarized in Table.1.

## 3.2 Outline of the numerical experiments

A steady state of temperature and velocity is quoted for 400 years of integration, after which time the dominant heat balances are approximately steady in the thermocline yet still evolving in the deepest level (recall the diffusive time $L^2/A_{DH} \sim 1000$ yrs). We believe that this integration time is sufficient for investigating the interdecadal variation of the horizontal temperature structure in the thermocline.

The experiments to investigate the variation of the horizontal temperature fields are executed by using this steady state as an initial condition. In the experiments, the ways changing the wind stress curl ($\partial\tau^x/\partial y$) are shown in Fig.8. In Experiment 1 (hereafter EX1), the magnitude of the wind stress is decreased. This decrease results in the uniform decrease in the magnitude of the wind stress curl on both subtropical and subpolar gyres.

The experiment 2 (hereafter EX2) is a counterpart of EX1; this is executed for the increase in the magnitude of the wind stress. This increase results in the increase in the magnitude of the wind stress curl on both subtropical and subpolar gyres.

These experiments are executed for the sudden change in the magnitude of the wind stress curl. The rate of change is 18% of the steady state value. This rate is referred to the observational evidence in Fig.4. The integration time of these experiments is 20 years. As a result of the numerical experiments, this time is sufficient for investigating most of the transient motions in the thermocline.

# 4 Preliminary considerations

In order to interpret the results of numerical experiments analytically, we employ two equations which is useful to describe the variation of the horizontal temperature structure in the thermocline of the interior region. In this section, we derive these equations according to our four-level model, and consider the dynamics in the interior region based on these equations. Furthermore, we consider briefly the dynamical response of the temperature structures at the eastern/western boundaries to the variation of the wind stress curl.

## 4.1 Dynamics based on the planetary geostrophic equations

In this paper, attention is directed to the interdecadal time-scale, and hence large-scale variability in the ocean, so that the time-dependent motions are quasi-geostrophic. According to this assumption, the governing equations shown in section 3.1 are rewritten as

$$-fv = -\frac{1}{\rho_0}\frac{\partial}{\partial x}p \tag{4.1.1}$$

$$fu = -\frac{1}{\rho_0}\frac{\partial}{\partial y}p \tag{4.1.2}$$

$$\frac{\partial}{\partial z}p = -\rho g \tag{4.1.3}$$

$$\frac{\partial}{\partial x}u + \frac{\partial}{\partial y}v + \frac{\partial}{\partial z}w = 0 \tag{4.1.4}$$

$$\frac{\partial}{\partial t}T + \frac{\partial}{\partial x}(uT) + \frac{\partial}{\partial y}(vT) + \frac{\partial}{\partial z}(wT) = A_{DH}\nabla_H^2 T + A_{DV}\frac{\partial^2}{\partial z^2}T + CA(T) \tag{4.1.5}$$

This system of equations are generally called the planetary geostrophic equations (e.g., Colin de Verdiére, 1988).

In the level model described by the planetary geostrophic equations, the vertical velocity shears are related to the horizontal temperature shears through the thermal wind relations. Thus, (4.1.1) and (4.1.2) by using (4.1.3) and (3.1.1) give

$$\boldsymbol{u}_1 - \boldsymbol{u}_2 = \frac{\lambda}{f}\boldsymbol{L}\{H_1T_1 + H_2T_2\} \tag{4.1.6}$$

$$\boldsymbol{u}_2 - \boldsymbol{u}_3 = \frac{\lambda}{f}\boldsymbol{L}\{H_2T_2 + H_3T_3\} \tag{4.1.7}$$

where $\lambda = (g\ \alpha)/(2\ \rho_0)$ is a constant, and $\boldsymbol{L}\{\ \} = (-\partial/\partial y,\ \partial/\partial x)$ is a vector operator. The subscripts denote the levels which are described in Fig.9.

Here, we define the total depth except the uppermost level $H = H_1 + H_2 + H_3$ and the thermocline depth $h = H_1 + H_2$. Hereafter, $H$ is simply called the total-depth, and $h$ is called the thermocline-depth. Then, (4.1.6)$\times(H_1/h - H_1/H)$+(4.1.7)$\times(H_3/H)$ and (4.1.7)$\times(H_2/h)$ give, respectively

$$\boldsymbol{u}' = \frac{H_3}{H}\frac{\lambda}{f}\boldsymbol{L}\left\{\Gamma + \frac{H_1H_2}{h}(T_1 - T_2)\right\} \tag{4.1.8}$$

$$\boldsymbol{u}'' = \frac{H_2}{h}\frac{\lambda}{f}\boldsymbol{L}\{\Theta\} \tag{4.1.9}$$

where

$$\boldsymbol{u}' = \frac{1}{h}\{(H_1\boldsymbol{u}_1 + H_2\boldsymbol{u}_2) - h\boldsymbol{U}\} \tag{4.1.10}$$

$$\boldsymbol{u}'' = \frac{H_2}{h}(\boldsymbol{u}_1 - \boldsymbol{u}_2) \tag{4.1.11}$$

$$\boldsymbol{U} = \frac{1}{H}(H_1\boldsymbol{u}_1 + H_2\boldsymbol{u}_2 + H_3\boldsymbol{u}_3) \tag{4.1.12}$$

and

$$\Gamma = H_1T_1 + H_2T_2 + H_3T_3 \tag{4.1.13}$$

$$\Theta = H_1T_1 + H_2T_2 \tag{4.1.14}$$

$\boldsymbol{u}'$ and $\boldsymbol{u}''$ represent two types of vertical velocity shear, and $\boldsymbol{U}$ represents the velocity averaged over the total-depth.

Above velocity components correspond to the following decompositions of a vertical velocity profile:

$$\begin{bmatrix} u_1 \\ u_2 \\ u_3 \end{bmatrix} = \boldsymbol{U}\begin{bmatrix} 1 \\ 1 \\ 1 \end{bmatrix} + \boldsymbol{u}'\begin{bmatrix} 1 \\ 1 \\ -\frac{h}{H_3} \end{bmatrix} + \boldsymbol{u}''\begin{bmatrix} 1 \\ -\frac{H_1}{H_2} \\ 0 \end{bmatrix} \tag{4.1.15}$$

The vertical profiles of these components are schematically shown in Fig.10. Hereafter, $\boldsymbol{U}$, $\boldsymbol{u}'$ and $\boldsymbol{u}''$ are called the velocity-structure-0, 1 and 2, respectively. The total-depth integrations of the velocity-structure-1 and 2 (hence, transports) are zero, respectively. Although these velocity components defined above do not correspond to the normal modes derived from the linear equations, these have similar structures to the normal modes. This decomposition is useful to analyze the non-linear system in this level model because of the direct connections with temperature fields. Namely, $\boldsymbol{u}''$ depends on the horizontal gradient of $\Theta$. Furthermore, if the second term on the right hand side of (4.1.8) is neglected (the validity of this approximation will be checked later by solutions of the numerical experiments), $\boldsymbol{u}'$ depends on the horizontal gradient of $\Gamma$. Thus, (4.1.8) is replaced by

$$\boldsymbol{u}' \approx \frac{H_3}{H}\frac{\lambda}{f}\boldsymbol{L}\{\Gamma\} \tag{4.1.16}$$

Sverdrup vorticity balance gives the velocity-structure-0 as $\beta V = fw_1/H$ in the interior region. Furthermore, $w_1$ is approximately equivalent to the Ekman pumping; $w_1 = -curl(\boldsymbol{\tau}/f)$. Therefore, the velocity-structure-0 depends only on the distribution of the Ekman pumping. On the other hand, the vertical-structure-1 and 2 depend on $\Gamma$ and $\Theta$, respectively. Therefore, the horizontal structures of $\Gamma$ and $\Theta$ determine the baroclinic

features in this model. Dynamically important variables in this level model are $\Gamma$, $\Theta$, $\boldsymbol{U}$, $\boldsymbol{u}'$ and $\boldsymbol{u}''$.

The equations to predict $\Gamma$ and $\Theta$ are obtained by using the temperature conservation equation (4.1.5). Integrating (4.1.5) over the total-depth and over the thermocline-depth give

$$\frac{\partial}{\partial t}\Gamma + \nabla\{\boldsymbol{u}_1 H_1 T_1 + \boldsymbol{u}_2 H_2 T_2 + \boldsymbol{u}_3 H_3 T_3\} + w_1 T_{01} = A_{DH}\nabla^2\Gamma + F^{01} + CA(T) \quad (4.1.17)$$

$$\frac{\partial}{\partial t}\Theta + \nabla\{\boldsymbol{u}_1 H_1 T_1 + \boldsymbol{u}_2 H_2 T_2\} + w_1 T_{01} - w_3 T_{23} = A_{DH}\nabla^2\Theta + F^{01} + F^{23} + CA(T) \quad (4.1.18)$$

where $T_{01}$ and $T_{23}$ are the temperatures at the interfaces between levels. According to the gird-spacing in our model, these variables are expressed as

$$T_{01} = \frac{T_0 + T_1}{2} \quad (4.1.19)$$

$$T_{23} = \frac{T_2 + T_3}{2} \quad (4.1.20)$$

In addition, $F^{01}$ and $F^{23}$ are the vertical eddy thermal fluxes between levels. These terms are given by

$$F^{01} = 2\ A_{DV}\frac{T_0 - T_1}{H_0 + H_1} \quad (4.1.21)$$

$$F^{23} = 2\ A_{DV}\frac{T_2 - T_3}{H_2 + H_3} \quad (4.1.22)$$

The advection terms in (4.1.17) and (4.1.18) are separated into the velocity-structure-0, 1 and 2, respectively, such that

$$\boldsymbol{u}_1 H_1 T_1 + \boldsymbol{u}_2 H_2 T_2 + \boldsymbol{u}_3 H_3 T_3 = \boldsymbol{U}\Gamma + h\boldsymbol{u}'(\frac{\Theta}{h} - T_3) + H_1\boldsymbol{u}''(T_1 - T_2) \quad (4.1.23)$$

$$\boldsymbol{u}_1 H_1 T_1 + \boldsymbol{u}_2 H_2 T_2 = (\boldsymbol{U} + \boldsymbol{u}')\Theta + H_1\boldsymbol{u}''(T_1 - T_2) \quad (4.1.24)$$

Here, we ignore the third term on the right hand side of (4.1.23) for simplicity. Then, (4.1.23) is replaced by

$$\boldsymbol{u}_1 H_1 T_1 + \boldsymbol{u}_2 H_2 T_2 + \boldsymbol{u}_3 H_3 T_3 \approx \boldsymbol{U}\Gamma + h\boldsymbol{u}'(\frac{\Theta}{h} - T_3) \quad (4.1.25)$$

The validity of the truncation of the velocity-structure-2 will be checked later by solutions of numerical experiments.

The substitutions of (4.1.16) and (4.1.14) into the second terms on the right hand side of (4.1.25) and (4.1.24) give, respectively

$$\frac{\partial}{\partial t}\Gamma + (\boldsymbol{A}\nabla)\Gamma = -W_1(T_{01} - \frac{\Gamma}{H}) + F^{01} + CA(T) + A_{DH}\nabla^2\Gamma \tag{4.1.26}$$

$$\frac{\partial}{\partial t}\Theta + (\boldsymbol{B}\nabla)\Theta = -W_1(T_{01} - \frac{\Theta}{h}) - W_3(\frac{\Theta}{h} - T_{23}) + F^{01} + CA(T) - F^{23} + A_{DH}\nabla^2\Theta \tag{4.1.27}$$

where

$$\boldsymbol{A} = \boldsymbol{U} + \boldsymbol{A}1 \tag{4.1.28}$$

$$\boldsymbol{B} = \{\boldsymbol{U} + \boldsymbol{u}'\} + \boldsymbol{B}1 \tag{4.1.29}$$

and

$$\boldsymbol{A}1 = \lambda\frac{hH_3}{H}\boldsymbol{L}\left\{\frac{\Theta/h - T_3}{f}\right\}$$

$$\boldsymbol{B}1 = \lambda\frac{H_1H_2}{h}\boldsymbol{L}\left\{\frac{T_1 - T_2}{f}\right\}$$

These equations are non-linear 1st-order partial differential equations of $\Gamma$ and $\Theta$, except the horizontal diffusions. Both $\boldsymbol{A}$ and $\boldsymbol{B}$ are composed of two terms; the first one is the horizontal advection, and the second one means the wave propagation which is explained below. The right hand sides of (4.1.26) and (4.1.27) represent the forcing terms, which are composed of the vertical heat advection, vertical heat diffusion, convection and horizontal diffusion.

The terms $\boldsymbol{A}1$ and $\boldsymbol{B}1$ are separated into two parts, namely

$$\boldsymbol{A}1 = -\lambda\frac{hH_3}{H}\frac{\beta}{f^2}\{(\Theta/h - T_3), 0\} + \lambda\frac{hH_3}{H}\frac{1}{f}\left\{\frac{\partial}{\partial y}(\Theta/h - T_3), -\frac{\partial}{\partial x}(\Theta/h - T_3)\right\} \tag{4.1.30}$$

$$\boldsymbol{B}1 = -\lambda\frac{H_1H_2}{h}\frac{\beta}{f^2}\{(T_1 - T_2), 0\} + \lambda\frac{H_1H_2}{h}\frac{1}{f}\left\{\frac{\partial}{\partial y}(T_1 - T_2), -\frac{\partial}{\partial x}(T_1 - T_2)\right\} \tag{4.1.31}$$

The first terms in the above equations correspond to the non-dispersive long baroclinic Rossby wave, which is generated by the mass convergence/divergence due to the $\beta$ effect.

On the other hand, the second terms are likely to represent the wave, which is generated by the heat convergence/divergence due to the vertical shear of geostrophic currents. The similar equation to (4.1.26) and (4.1.27) has been used in order to study the thermocline structure in the steady subtropical gyre; i.e., Cushuman-Roisin (1984) to continuously stratified ocean, Luyten and Stommel (1986) to 2.5-layer model, and Huang (1993) to two-level model with a constant temperature in the lower level. However, the equations of these previous studies do not have the effect which corresponds to the second term in (4.1.30) or (4.1.31). Thus, we briefly compare the layer model with the level model under the planetary geostrophic equations. The 2-layer model and 2.5-layer model do not have the mass convergence/divergence due to ageostrophic effects except the $\beta$ effect, so that these models have only non-dispersive long baroclinic Rossby wave. However, The 3.5-layer model has the mass convergence/divergence due to the vertical shear of geostrophic currents, which seems to represent the vortical wave caused by potential vorticity gradients. This wave in the 3.5-layer model might be the counterpart of the wave which is represented by the second term in (4.1.30) or (4.1.31), although the layer and level models cannot be exactly compared through the reason that potential vorticity is not conserved in the level model. How important are the second terms in (4.1.30) and (4.1.31)? The numerical experiments will demonstrate that the second term propagates heat with the same significance as the first term. Therefore, it is considered that the second term is essential to predict the variation in the horizontal temperature fields.

The equations (4.1.26) and (4.1.27) predict the temporal and spatial variations of $\Gamma$ and $\Theta$ fields, respectively. $\Gamma$ and $\Theta$ advect/propagate along characteristics [1] formed by $\boldsymbol{A}$ and $\boldsymbol{B}$ based on these equations. Therefore, the horizontal structures of $\Gamma$ and $\Theta$ can be diagnosed by the characteristics which are drawn by using the solutions of numerical model.

Our interest in this study is the dynamical response of the horizontal temperature fields

[1]Characteristics mean paths, along which $\Gamma$ or $\Theta$ propagates/advects; i.e., stream lines drawn by $\boldsymbol{A}$ or $\boldsymbol{B}$.

in the thermocline to the decadal variation of the wind stress curl. In the system derived above, the horizontal structure of $\Theta$ represents the horizontal temperature structure in the thermocline. Therefore, (4.1.27) gives the intrinsic considerations concerned with the variations of the horizontal temperature structure in the thermocline.

## 4.2 The basic equations for the analytical method

In this subsection, we consider the long-term variation of $\Theta$ on the basis of (4.1.27). First, the perturbation equation of (4.1.27) is derived to clarify the mechanism by which variations of $\Theta$ occur. The perturbation method can be applied, when the non-linearity in the temperature variations is weak. The validity of this method will be checked later through the comparison of EX1 with EX2. Equation (4.1.27) is briefly rewritten as

$$\frac{\partial}{\partial t}\Theta + (\boldsymbol{B}\nabla)\Theta = F \tag{4.2.1}$$

where F represents the forcing terms on the right hand side of (4.1.27).

All variables are divided into the steady component ($\{\quad\}_0$) and time-dependent component ($\{\quad\}'$), namely

$$\begin{aligned} \Theta &= \Theta_0 + \epsilon\Theta' \\ \boldsymbol{B} &= \boldsymbol{B}_0 + \epsilon\boldsymbol{B}' \\ F &= F_0 + \epsilon F' \end{aligned}$$

where $\epsilon \ll 1$. Then, the equation consisting of the order ($\epsilon$) terms is given by

$$\frac{\partial}{\partial t}\Theta' + (\boldsymbol{B}'\nabla)\Theta_0 + (\boldsymbol{B}_0\nabla)\Theta' = F' \tag{4.2.2}$$

This equation describes the time-dependent $\Theta'$. The local time-variation of $\Theta'$ is caused by the variation of characteristics, the advection/propagation of $\Theta'$ along characteristics, and the variation of the forcing terms. Here, the variation of characteristics is given by

$$\boldsymbol{B}' = \{\boldsymbol{U} + \boldsymbol{u}'\}' + \lambda\frac{H_1 H_2}{h}\boldsymbol{L}\left\{\frac{T_1 - T_2}{f}\right\}' \tag{4.2.3}$$

The variation of $\boldsymbol{U}$ is caused by the Ekman pumping change based on the Sverdrup balance, and the variation of $\boldsymbol{u}'$ is caused by the $\Gamma$ variation through the thermal wind relation. In addition, the variation of the wave propagation term is generated by the variation of the stratification in the thermocline. The $\Theta$ variation is strongly related to the $\Gamma$ variation through the variation of $\boldsymbol{u}'$.

By using the same method for $\Theta$, the perturbation equation of $\Gamma$ is derived from (4.1.26), such that

$$\frac{\partial}{\partial t}\Gamma' + (\boldsymbol{A}'\nabla)\Gamma_0 + (\boldsymbol{A}_0\nabla)\Gamma' = G' \tag{4.2.4}$$

where $G'$ is the variation of the forcing terms. This equation describes the time-dependent $\Gamma'$.

The equations (4.2.3) and (4.2.4) are the basic equations to describe the temporal and spatial variations of $\Theta$ and $\Gamma$, respectively. We will analyze these variations based on (4.2.3) and (4.2.4) in section 5.

## 4.3 Dynamics at the eastern/western boundaries

The response in the coastal region to the variation of the wind stress pattern has been studied for the linear problem. For example, Gill and Clarke (1974) investigated the coastal upwelling induced by the changing wind patterns on the f-plane ocean, and then Anderson and Gill (1975) solved this problem on the mid-latitude $\beta$-plane ocean. Furthermore, Davey (1983) studied the baroclinic response to the thermal forcing on the mid-latitude $\beta$-plane ocean by using two-level model. In this subsection, we mainly consider the linear response of $\Gamma$ along the eastern/western boundaries on the f-plane ocean to the variation of the wind stress curl based on the four-level model.

We derive the linear equation concerned with the time-dependent $\Gamma$ on the f-plane ocean. The governing equations in section 3.1 are simplified to

$$-fv = -\frac{1}{\rho_0}\frac{\partial}{\partial x}p \tag{4.3.1}$$

$$\frac{\partial}{\partial t}v + fu = -\frac{1}{\rho_0}\frac{\partial}{\partial y}p \tag{4.3.2}$$

$$\frac{\partial}{\partial z}p = -\rho g \tag{4.3.3}$$

$$\frac{\partial}{\partial x}u + \frac{\partial}{\partial y}v + \frac{\partial}{\partial z}w = 0 \tag{4.3.4}$$

$$\frac{\partial}{\partial t}T + \frac{\partial}{\partial x}(uT) + \frac{\partial}{\partial y}(vT) + \frac{\partial}{\partial z}(wT) = 0 \tag{4.3.5}$$

The cross-differentiation of (4.3.1) and (4.3.2) with f=constant yields

$$\frac{\partial^2}{\partial t \partial x}v + f(\nabla_H \boldsymbol{u}) = 0 \tag{4.3.6}$$

The velocity-structure-1($\boldsymbol{u}'$) is dealt with independently, under the assumption that the velocity-structure-1 is approximately equal to the 1st baroclinic model. The substitution of (4.1.16) into (4.3.6) gives

$$\nabla_H(h\boldsymbol{u}') = -\frac{1}{f^2}\lambda\frac{hH_3}{H}\frac{\partial^3}{\partial t \partial^2 x}\Gamma \tag{4.3.7}$$

The equations (4.1.17) except the horizontal diffusion and (4.1.25) give the linearized $\Gamma$ conservation, namely

$$\frac{\partial}{\partial t}\Gamma + \hat{\Gamma}\nabla_H(h\boldsymbol{u}') = -W_1(T_{01} - \frac{\Gamma}{H}) + F^{01} + CA(T) \tag{4.3.8}$$

where $\hat{\Gamma} = \Theta/h - T_3$ is assumed to be a constant along the coast. Substituting of (4.3.7) into (4.3.8) gives

$$\frac{\partial}{\partial t}\Gamma - L^2\frac{\partial^3}{\partial t \partial^2 x}\Gamma = K \tag{4.3.9}$$

where

$$L^2 = -\frac{1}{f^2}\lambda\frac{hH_3}{H}\hat{\Gamma} \tag{4.3.10}$$

$$K = -W_1(T_{01} - \frac{\Gamma}{H}) + F^{01} + CA(T) \tag{4.3.11}$$

The normal flow at the eastern/western walls is zero. Thus, (4.3.2) gives the boundary conditions at the eastern/western boundaries such that

$$fu = -\frac{\partial}{\partial t}v - \frac{1}{\rho_0}\frac{\partial}{\partial y}p = 0 \tag{4.3.12}$$

This equation is applied for the velocity-structure-1, then

$$\frac{\partial^2}{\partial t \partial x}\Gamma + f\frac{\partial}{\partial y}\Gamma = 0 \tag{4.3.13}$$

The similar equations to (4.3.9)-(4.3.11) and (4.3.13) were derived by Davey (1983) for two-level model with thermal forcing.

This system of equations is analytically solved for the given initial and forcing conditions (Gill and Clarke, 1974). The solution near the eastern boundary ($x = X_E$) is

$$\Gamma = \int_0^T K(y - Lft)dt\ exp\{(x - X_E)/L\} + K(y)t\{1 - exp\{(x - X_E)/L\}\} \tag{4.3.14}$$

where $T$ is an arbitrary time. On the other hand, the solution near the western boundary ($x = 0$) is

$$\Gamma = \int_0^T K(y + Lft)dt\ exp(-x/L) + K(y)t\{1 - exp(-x/L)\} \tag{4.3.15}$$

At the eastern and western boundaries, the solutions are reduced to

$$\Gamma = \int_0^T K(y - Lft)dt \tag{4.3.16}$$

$$\Gamma = \int_0^T K(y + Lft)dt \tag{4.3.17}$$

where $Lf$ is the Kelvin wave speed. The variation of $\Gamma$ depends on the information carried by the Kelvin wave. As for the response of $\Gamma$ to the variation of wind stress curl, the dominant change in the forcing terms described by (4.3.11) is considered to be the change of the Ekman Pumping ($w_1$).

In the linear system, the variation of $\Theta$ along the coast is described by the same equation as that for $\Gamma$ except the Kelvin wave speed. However, if the non-linearity, such as the change in horizontal heat advection, is important, the coastal variation of $\Theta$ could be significantly different from that of $\Gamma$. The numerical experiments in section 5 will demonstrate that the variation of $\Theta$ at the subtropical western boundary is affected by the non-linear advection.

# 5 Results of numerical experiments

## 5.1 The comparison of the North Atlantic with the model results

Steady temperature distributions in the model are compared with those in the North Atlantic subtropical-subpolar system. Figures 11a and 11b show the horizontal distributions of the vertically averaged temperature and temperature stratification in the thermocline of the North Atlantic, respectively. On the other hand, Figures 11c and 11d show the horizontal distributions of $\Theta$ [2] and $T_1 - T_2$ in the thermocline of the model, respectively.

The characteristic features in the temperature fields shown in Fig.11a are summarized as follows: 1) the strong horizontal temperature gradients in the Gulf Stream system; 2) the temperature structure related to the subtropical front, i.e., the turns of isotherms from southward to eastward direction in the subtropical interior region (indicated by a dashed line in Fig.11a); 3) the isotherms which extend northward with strong gradients due to the North Atlantic Current, the eastward turns of these isotherms in the northern subpolar gyre, and the homogeneous temperature fields west of these isotherms in the subpolar gyre. Above three characteristic features, which are considered to be the main structures in the North Atlantic, are clearly identified in the $\Theta$ field (Fig.11c).

On the other hand, the characteristic features in the temperature fields shown in Fig.11b are summarized as follows: 1) the strong stratification along both the southern perimeter of the subtropical gyre and the Gulf Stream system; 2) the weak stratification in both the recirculation region and the northeastern region of the subtropical gyre; 3) the relatively strong stratification in the central subpolar gyre, and the weak stratification in both the eastern and western subpolar gyres. Above three characteristic features in the stratification in the North Atlantic thermocline are clearly identified in the $T_1 - T_2$ field

[2] $\Theta/h$ and $\Gamma/H$ are simply termed $\Theta$ are $\Gamma$ throughout this paper, respectively. Notice that terms in figure captions are correct.

(Fig.11d).

As mentioned above, the model reproduces the main thermal structures of the subtropical-subpolar system in the North Atlantic, although the complete agreement cannot be obtained because of the simplification of the model ocean, such as the coast line, bottom topography and wind stress distribution.

Next, the horizontal pattern of the temperature structure change in the model thermocline, which is caused by the sudden decrease in the magnitude of the wind stress curl, is checked with the observed horizontal pattern in the North Atlantic shown by Levitus (1989).

Figure 12a shows the difference between the $\Theta$ field after the 20 years of integration and that in the steady state. As shown in Fig.12a, temperature decreases in the northwestern subtropical gyre and weakly increases in the eastern subtropical gyre except the southeastern corner. Figure 11c indicates that these two regions are separated by a dashed curve in Fig.11c; this curve is characterized by the points where the isotherms turn from southward to eastward direction in the subtropical interior region. Furthermore, significant decrease of $\Theta$ is seen to occur south of the extension of the subtropical western boundary current.

On the other hand, Fig.12a shows that $\Theta$ increases in the southwestern subpolar gyre except the western boundary current, and decreases in the northeastern subpolar gyre. Figure 11b indicates that above two regions can be separated by the line connecting the points at which isotherms of $\Theta$ turn from northward to the eastward direction.

Above spatial patterns of the temperature structure change agree well with those of the observed change at intermediate depths shown by Levitus(1989) (see Fig.1a in section 5.1), except in the southeastern corner of the subtropical gyre and the western boundary current of the subpolar gyre. In two regions above, the model predicted temperature is affected by the temperature variation on the opposite boundaries at each gyre, because the Kelvin wave propagates along the closed boundary. This results in the disagreements between the model predicted temperature and observed one.

Based on the comparison between the observations and model solutions, we believe that the weakened wind stress curl over the North Atlantic could play an important role in generating the temperature variation observed in the North Atlantic. The numerical model has demonstrated that the uniformly weakened wind stress curl causes the temperature variation with the different tendencies between the western and eastern domains. In the following subsections, the mechanism which generates this spatial pattern is clarified.

## 5.2 The comparison of EX1 with EX2

The variation of the $\Theta$ field for EX1 is compared with that for EX2. Figures 12a and 12b show the difference between the $\Theta$ field after the 20 years of integration and that in the steady state for EX1 and EX2, respectively. Comparison between Fig.12a and Fig.12b shows that there is no major difference between EX1 and EX2 in both spatial pattern and amplitude of the $\Theta$ difference, except the amplitude with reversed sign.

As mentioned in section 4.2, the variation of $\Theta$ is analyzed by using two perturbation equations (4.2.4) and (4.2.2), which are derived assuming the weak non-linearity of the temperature variation. If this assumption is appropriate, the response of $\Theta$ field for EX1 should be reversal of that for EX2. The similarity between the $\Theta$ difference for EX1 (Fig.12a) and that for EX2 (Fig.12b) indicates the validity of this assumption.

The weak non-linearity of the temperature variation suggests that the oceanic response to the sudden change in the wind stress curl is similar to its response to the gradual change in the wind stress curl, which is much realistic.

In the following subsections, we will analyze the time-dependent motions for EX1, because time-dependent motion for EX2 is essentially the same as that for EX1.

## 5.3 The steady state of $\Gamma$ and $\Theta$ fields

The steady state solutions are first examined in this subsection before discussing the time-dependent solutions. Figures 13a and 13b show the $\Gamma$ and $\Theta$ fields, respectively,

whereas, Figures 13c and 13d show the velocity-structure-1($\boldsymbol{u}'$) and velocity-structure-2($\boldsymbol{u}''$), respectively. The flow pattern of the velocity-structure-1 (Fig.13c) is along isotherms of $\Gamma$ (Fig.13a), indicating that the approximation used in (4.1.16) is appropriate. The flow pattern of the velocity-structure-2 is also along isotherms of $\Theta$

The horizontal structure of the $\Gamma$ field is nearly the same as that of the transport stream function (Fig.13e) representing the linear wind driven circulations in the subtropical-subpolar system, except the width of the western boundary current in the subpolar gyre. In contrast to the width of the western boundary current in the subtropical gyre which almost corresponds to the Munk scale ($\sqrt[3]{A_{MH}/\beta}$ $\sim$140km, hence the width of the real boundary current is two or three times this scale), the width of the western boundary current in the subpolar gyre is by a factor of about two lager than that in the subtropical gyre (Fig.13a and Fig.13c). This is explained in terms of characteristics of $\Gamma$ given by (4.1.28). Figure 14a shows characteristics of $\Gamma$ drawn by using the numerical model in the steady state. We can see that the characteristics of $\Gamma$ emanating from the eastern boundary cannot reach the western boundary in the subpolar gyre, because wave propagation is significantly inhibited by advection effects (velocity-structure-0). Therefore, the baroclinic current at the western boundary in the subpolar gyre cannot be scaled by $\sqrt[3]{A_{MH}/\beta}$, but may be scaled by the boundary layer width which depends on the advection and horizontal diffusion of $\Gamma$ (see (4.1.26)). Namely, this width is represented by $A_{DH}/U \geq$100Km as $A_{DH} = 5 \times 10^6$ cm$^2$s$^{-1}$ and $U \leq 0.5$ cms$^{-1}$. This type of boundary layer was first discussed by Bryan and Cox (1968).

On the other hand, the $\Theta$ field is considerably different from the $\Gamma$ field. The characteristics of $\Theta$ are shown in Fig.14b. The subtropical front is located just on the boundary between two families distinguished by the different starting points of characteristics. This is consistent with the generation mechanism that the subtropical front is formed by the intersect of the characteristics (Cushuman-Roisin, 1984; Kubokawa, pers. comm., 1995). The dashed curve in Fig.11c, which indicates the boundary between the western domain with temperature decrease and the eastern domain with temperature increase, is identi-

fied at the eastern end of the subtropical front. On the other hand, in the subpolar gyre the line connecting the points at which isotherms turn northward to eastward direction (Fig.11c) does not fit the boundary between two families of characteristics of $\Theta$ , but this fits the western edge of the region suffered from the active convection (Fig.15).

## 5.4 The immediate response of $\Gamma$ and $\Theta$ fields

With the sudden decrease in the magnitude of the wind stress curl, Ekman transport and Ekman pumping change all over the basin within the inertial period $(1/f)$, namely about one day in the mid-latitude ocean. Furthermore, the barotropic velocity fields are adjusted all over the basin, after the barotropic long Rossby wave emanating from the eastern boundary reaches the western boundary. Since the zonal basin width is about 4000km and its wave speed in the mid-latitude is about 100m/s, it takes about one day for this wave to across the basin. The 1st baroclinic Kelvin wave changes the temperature and velocity structures at the eastern boundary. Since the speed of this wave is about 2m/s, it propagates along the eastern boundary from the southern end to the northern end (4500km) in one month. Thus, the $\Gamma$ and $\Theta$ fields at 30 day after the sudden decrease in the magnitude of wind stress curl are shown for the immediate response of the ocean.

The immediate change in the $\Gamma$ field (Fig.16a) is first analyzed. The immediate change in $\Gamma$ over the interior region is described by (4.2.4). The $\Gamma'$ field locally responds as

$$\frac{\partial}{\partial t}\Gamma' \sim G' \tag{5.4.1}$$

where

$$G' = W_1'(\frac{\Gamma}{H} - T_{01})_0 + (W_1)_0(\frac{\Gamma}{H} - T_{01})' + F^{01'} + CA(T)' + A_{DH}\nabla^2\Gamma' \tag{5.4.2}$$

The first term on the right hand side of (5.4.2) is most dominant, representing the change in the vertical heat advection associated with the change in the Ekman pumping. As shown in Fig.16a, this effect results in the zonally uniform and meridionally sinusoidal-type decrease of $\Gamma$ in the subtropical interior region. On the other hand, $\Gamma$ in the subpolar

interior region increases with the smaller amplitude than that in the subtropical interior region, because the stratification and the amplitude of the Ekman pumping in the subpolar gyre are weaker and smaller than those in the subtropical gyre.

The other dominant term of $G'$ is the change in convection. As shown in Fig.16a, the highest $\Gamma$ anomaly is formed in the western region just on the boundary between the subtropical and subpolar gyres. This anomaly is caused by the weakened convection associated with the decrease in the southward Ekman transport. Above process is verified by the fact that the region with the highest $\Gamma$ anomaly (Fig.16a) corresponds to the region suffered from active convection (Fig.15).

$\Gamma$ decreases at the eastern boundary of the subpolar gyre (Fig.16a), because the coastal Kelvin wave propagates the $\Gamma$ anomaly from the subtropical region to the subpolar region. The decrease of $\Gamma$ along the subpolar eastern boundary intensifies the zonal gradient of $\Gamma$ along the boundary. According to the thermal wind relation, the velocity field along the eastern boundary is northward in the subtropical gyre and southward in the subpolar gyre (Fig.16b).

The $\Theta$ field responses immediately by the same mechanism as the $\Gamma$ field except in the western boundary current of the subtropical gyre (Fig.16c). $\Theta$ in the northern half of the subtropical western boundary current decreases much more than that in the subtropical interior region, because of the reduction in the horizontal heat advection due to the weakened velocity-structure-1. Therefore, the change in the velocity-structure-2 is northward in the subtropical western boundary current (Fig.16d). The $\Theta$ variation in the subtropical western boundary current is dominated by the non-linear process.

## 5.5 The long-term response of $\Gamma$ field

The equation (4.2.3) shows that the change in characteristics of $\Theta$ is caused by the variation in the velocity-structure-1, which is related to the time-dependent $\Gamma$. Thus, before discussing the time-dependent $\Theta$, we will analyze the time-dependent $\Gamma$ in this subsection.

Figures 17a and 17b show the time series of the $\Gamma$ and $\boldsymbol{u}'$ anomaly fields for 4 years of integration, respectively. These figures show that the $\Gamma$ field is adjusted gradually from the eastern boundary to the western boundary, after the $\Gamma$ field has responded locally. A meridionally extending stripe of the intensive velocity anomalies is identified in each picture of Fig.17b. These stripes show fronts of the westward propagating wave which has been excited immediately at the eastern boundary. Figure 14a shows that this wave front propagates westward along characteristics of $\Gamma$.

The process mentioned above is represented by the following equations derived from (4.2.4);

$$\frac{\partial}{\partial t}\Gamma' \sim G' \quad \text{for the local response} \tag{5.5.1}$$

$$(\boldsymbol{A}_0\nabla)\Gamma' \sim G' \quad \text{for the remote response} \tag{5.5.2}$$

These equations represent the linear response of the $\Gamma$ field, which is similar to that in Gill and Anderson (1975); i.e., the vertical shift of the thermocline caused by the local Ekman pumping change and the long Rossby wave propagation from the eastern boundary. However, characteristics in Fig.14a are significantly different from the zonally extending characteristics which are drawn by the long Rossby wave in Gill and Anderson (1975), because of the advection and the other wave in (4.1.28).

The equation (4.1.28) shows that $\boldsymbol{A}_0$ are composed of the advection and two types of waves; one is the non-dispersive long Rossby wave (hereafter called type-1 wave), and the other is the wave caused by the heat convergence/divergence due to the vertical shear of geostrophic currents (hereafter called type-2 wave). The contributions of the type-2 waves to characteristics of $\Gamma$ and $\Theta$ are examined. Figures 18a and 18b show the characteristics of $\Gamma$ and $\Theta$ without the type-2 waves, respectively. Comparison between Fig.14a and Fig.18a shows that the propagating course and time in characteristics of $\Gamma$ (Fig.14a) are significantly different from those without the type-2 wave (Fig.18a). The difference between Fig.14a and Fig.18a indicates the importance of the type-2 wave for the time-dependent $\Gamma$. On the other hand, comparison between Fig.14b and Fig.18b shows

that the propagating course and time of characteristics of $\Theta$ (Fig.14b) is similar to those without the type-2 wave (Fig.18b), except in the eastern domain of subtropical gyre. The similarity between Fig.14b and Fig.18b is based on the reason why the advection effects mainly determine characteristics of $\Theta$.

More long-term response of $\Gamma$ is examined. Figure 19 shows the time series of the $\Gamma$ anomaly fields for 20 years of integration. The variation of the $\Gamma$ field at 5 year (Fig.19a) shows the decrease of $\Gamma$ all over the subtropical gyre and the increase of $\Gamma$ over the subpolar gyre except its perimeter. At the perimeter of the subpolar gyer, $\Gamma$ decreases through the coastal Kelvin wave. The time series of $\Gamma$ anomaly fields from 5 to 20 year (Fig.19b, c, d) clearly show that adjustment occurs in the region where the characteristics of westward propagating wave pass by, while the variation of $\Gamma$ continues in the subpolar western region where the characteristics of the westward propagating wave cannot invade. The adjustment in the $\Gamma$ field in the subpolar western region is considered to occur under the effects of the horizontal diffusion (Fig.20).

## 5.6 The long-term response of $\Theta$ field

The dynamical response of the horizontal temperature field in the thermocline, i.e., the $\Theta$ field, is described. In this subsection. we focus on the mechanism to generate the temperature change with different tendencies between the western and eastern domains in both subtropical and subpolar gyres.

Figure 21 shows the time series of the $\Theta$ anomaly fields for 4 years of integration. Figure 21 demonstrates that the $\Theta$ anomalies move from east to west, after the $\Theta$ field has responded locally. Comparison between the time series of the $\Theta$ anomaly fields (Fig.21) and that of $\boldsymbol{u}'$ anomaly fields (Fig.17b) shows that the spatial pattern of the $\Theta$ anomaly fields changes in the region where the westward propagating wave of $\Gamma$ has passed. The $\Theta$ anomaly field at 4 year (Fig.17d) shows that $\Theta$ decreases intensively in the northwestern subtropical gyre and $\Theta$ increase weakly in the southeastern subtropical gyre, whereas $\Theta$ increase in the southwestern subpolar gyre and decrease in the northeastern subpolar

gyre.

The process mentioned above is dynamically described by the following equations derived from (4.2.2) and (4.2.3);

$$\frac{\partial}{\partial t}\Theta' \sim F' \quad \text{for the local response} \tag{5.6.1}$$

$$\frac{\partial}{\partial t}\Theta' \sim -(\boldsymbol{B}'\nabla)\Theta_0 - (\boldsymbol{B}_0\nabla)\Theta' + F' \quad \text{for the remote response} \tag{5.6.2}$$

where

$$\boldsymbol{B}' = \{\boldsymbol{U} + \boldsymbol{u}'\}' + \lambda\frac{H_1H_2}{h}\boldsymbol{L}\left\{\frac{T_1 - T_2}{f}\right\}' \tag{5.6.3}$$

The long-term response of $\Theta$, hence the remote response described by (5.6.2), is generated through three mechanisms; the change in characteristics, advection/propagation of the $\Theta$ anomaly along characteristics and the change in forcing. The dominant factor to change characteristics is examined by estimating each term in (5.6.3) (Fig.22). Figure 22 shows that the change in the velocity-structure-1 ($\boldsymbol{u}'$) (Fig.22b) dominates the change in characteristics all over the basin except near the boundary between the subtropical and subpolar gyres. Near the gyre boundary, the change of the wave propagation term (Fig.22c), in adding to the change in the velocity-structure-1, contributes the change in characteristics, because the change in convection modifies temperature stratification. The dominant factor to change characteristics of $\Theta$ in (5.6.3) is mainly the change in the velocity-structure-1.

Based on the above process, the dynamical response is summarized as follows: First, the $\Theta$ field varies all over the basin through the vertical shift of thermocline associated with the Ekman pumping change. Then, characteristics of $\Theta$ are modified mainly through the change in the velocity-structure-1, which is caused by the $\Gamma$ anomaly propagating from the eastern boundary. The change in characteristics of $\Theta$ generates locally the $\Theta$ anomalies with different tendencies between the western and eastern domains; i.e., 1) the intensive $\Theta$ decrease south of the extension of the subtropical western boundary current, 2) the weak $\Theta$ increase near the subtropical front, 3) the intensive $\Theta$ increase north of the extension of the subtropical western boundary current, and 4) the $\Theta$ decrease in the northeastern

subpolar gyre. The geographical feature of the formation areas of $\Theta$ anomalies depends on the steady $\Theta$ structure, which is maintained by the wind stress and surface buoyancy flux. The generated $\Theta$ anomalies propagate simultaneously along the characteristics of $\Theta$. In the subtropical gyre, the propagation of the $\Theta$ anomalies intensifies the different tendencies between the western and eastern domains, because characteristics of $\Theta$ are consisted of two families which is separated by the subtropical front. In the subpolar gyre, the propagation of $\Theta$ weakens gradually the contrast of the $\Theta$ change between the western and eastern domains, because characteristics extend from only southwestern boundary.

Figure 23 shows more long-term variation of $\Theta$ anomaly fields for 20 years of integration. This figure indicates that the $\Theta$ fields vary with significant magnitude until 10 year. The adjustment of the $\Theta$ variation is examined by estimating each term on the right hand side of (5.6.2). Here, the change in forcing in (5.6.2) is given by

$$\begin{aligned} F' &= -W_1'(T_{01} - \frac{\Theta}{h})_0 - W_3'(\frac{\Theta}{h} - T_{23})_0 - (W_1)_0(T_{01} - \frac{\Theta}{h})' - (W_3)_0(\frac{\Theta}{h} - T_{23})' \\ &\quad + F^{01\prime} + CA(T)' - F^{23\prime} + A_{DH}\nabla^2\Theta' \end{aligned} \tag{5.6.4}$$

Figure 24 shows the dominant terms in (5.6.2) after 10 years of integration. The heat balances in the eastern domains of the subtropical and subpolar gyres are as follows: at the southeastern subtropical gyre, the cooling caused by the upward Ekman pumping anomalies (Fig.24c, d) is balanced mainly by the heating caused by the change in characteristics (Fig.24a) and the advection/propagation of the $\Theta$ anomalies along characteristics (Fig.24b); at the northeastern subpolar gyre, the cooling caused by the change in characteristics (Fig.24a) is balanced mainly by the heating caused by the advection/propagation of the $\Theta$ anomalies (Fig.24b). On the other hand, The heat balances in the western domains of the subtropical and subpolar gyres are as follows: at the northwestern subtropical gyre, the cooling caused by the change in characteristics (Fig.24a) and the advection/propagation of $\Theta$ anomalies (Fig.24b) is balanced by the heating caused by the downward velocity anomalies (Fig.24d) and the horizontal diffusion (Fig.24e); at the

southwestern subpolar gyre, the heating caused by the change in characteristics (Fig.24a) and the advection/propagation of $\Theta$ anomalies (Fig.24b) is balanced by the cooling caused by the upward velocity anomalies (Fig.24d) and the horizontal diffusion (Fig.24e).

In the contrast to the heat balances in the eastern domains, in the western domains the forcing change associated with the Ekman pumping anomaly (Fig.24c), the change in characteristics (Fig.24a), and the advection/propagation of the $\Theta$ anomalies (Fig.24b) are not in balance. Therefore, the variation of the $\Theta$ field continues much longer in the western domains than in the eastern domains (see Fig.23).

## 5.7 The variation of the meridional circulation

The subtropical-subpolar system in the model is driven by the wind stress and surface heat flux. Therefore, the meridional circulation is consisted of the Ekman cell due to the wind stress and the thermal cell due to the surface heat flux. In this subsection, we discuss on the variation of the meridional circulation caused by the change in the magnitude of the wind stress curl.

Figure 25a shows the steady meridional circulation, which is derived from zonal integration of the meridional velocity at each level. In this figure, the Ekman cell corresponds to a remarkable cell, which is related to both the Ekman transport in the Ekman layer and its conservation flow in the upper thermocline. On the other hand, the thermal cell corresponds to a weak cell, which is related to both the northward transport in the upper thermocline and the southward transport in the lower thermocline and deepest level.

Figure 25b shows the meridional circulation anomaly at 20 years of integration caused by the weakened wind stress curl (for EX1). Figure 25b demonstrates a single anomaly cell, which is formed by both the northward transport anomaly in the Ekman layer and the southward transport anomaly in the lower thermocline and deepest level. Here, the northward transport anomaly in the Ekman layer completely corresponds to the Ekman transport anomaly given by $\tau_x/f$. The single anomaly cell is not ascribed to the linear response of the meridional circulation, because the structure of the anomaly field is dif-

ferent from that of the steady field. The single anomaly cell is based on the combined effects of the weakened Ekman cell and the intensified thermal cell.

On the other hand, Fig.25c shows the meridional circulation anomaly at 20 years of integration caused by increase in the magnitude of the wind stress curl (for EX2). Comparison between Fig.25b and Fig.25c shows that the meridional circulation anomaly for EX2 is completely the reversal of that for EX1.

The structure of the meridional transport anomaly depends on the change in the temperature field. In order to clarify the relation between the meridional transport anomaly and the change in the temperature field, we employ the thermal wind relations described by (4.1.16) and (4.1.9). The equations (4.1.16) and (4.1.9) are zonally integrated, respectively, and then

$$\int_{Xw}^{Xe} v' dx = \frac{H_3}{H}\frac{\lambda}{f}\{\Gamma\,|_{Xe} - \Gamma\,|_{Xw}\} \tag{5.7.1}$$

$$\int_{Xw}^{Xe} v'' dx = \frac{H_2}{h}\frac{\lambda}{f}\{\Theta\,|_{Xe} - \Theta\,|_{Xw}\} \tag{5.7.2}$$

where $X_e$ and $X_w$ denote the eastern boundary and the western boundary, respectively. The meridional transports of each component are determined by only temperatures in the eastern and western boundaries.

Figure 26a shows three components of the steady meridional transport, and Fig.26b shows the anomalies of three components at 20 years of integration for EX1. These figures demonstrate that the velocity-structure-2 varies so as to intensify the thermal circulation. Figure 27a shows the difference between the $\Gamma$ anomaly in the eastern boundary and that in western boundary, whereas Fig.27b shows the difference between the $\Theta$ anomaly in the eastern boundary and that in the western boundary. We can see that the profiles shown in Fig.27a and Fig.27b are consistent with the anomalies of the velocity-structure-1 (Fig.26a) and velocity-structure-2 (Fig.26b), respectively. It is shown that the significant decrease of $\Theta$ in the subtropical western boundary leads to the intensification of the thermal circulation for the velocity-structure-2. This intensive decrease of $\Theta$ in the subtropical western boundary is caused by the non-linear effects associated with the reduction in the

velocity-structure-1 (see Fig.16 for the immediate response and Fig.19 for the long-term response). The horizontal structure of change in the velocity-structure-2 after 20 years of integration is shown in Fig.28. This figure shows that in response to the weakened wind stress curl the velocity-structure-2 changes so as to intensify the western boundary current.

# 6 Discussion

The horizontal spatial pattern of temperature change in the thermocline caused by the weakened wind stress curl has been predicted by a simple numerical model. We have shown in section 4.1 that the horizontal spatial pattern of the model predicted temperature change is similar to that of the observed interdecadal change in the thermohaline structure at intermediate depths of the North Atlantic, which was reported by Levitus (1989). In particular, we have pointed out that the observed relation of the horizontal spatial pattern of temperature change to the mean horizontal temperature structure is well reproduced in the model. The agreement between the model predicted temperature change and the observed one indicates that the weakened wind stress curl over the subtropical-subpolar gyres played an important role in generating the observed interdecadal change in the North Atlantic. However, the numerical model used in this study is simplified; it assumes flat bottom, mid-latitude closed basin, and lower vertical resolution. Thus, it is worth discussing several problems arising from the simplification of the model.

Our numerical model ignores the bottom topography, such as the mid-Atlantic ridge, which is important for the dynamics in the North Atlantic. The bottom topography generates the topographic Rossby wave through the topographic $\beta$ effect, and mainly results in the change in barotropic flow field. Therefore, the bottom topography modifies the temporal and spatial structure of characteristics formed by combined effects of advection and wave propagation (see Fig.14). Further study is necessary to investigate to what extent the bottom topography modifies the temporal and spatial structure of

characteristics, because horizontal temperature variations in the thermocline depend on the structure of characteristics. In addition, the bottom topography generates the bottom pressure torque (called JEBAR), which might cause the temporal variation of transports when density structure near the bottom changes temporally. The change of transports caused by JEBAR leads to the change in the horizontal advection of heat and salt so that the thermohaline structure in the thermocline might be modified. Greatbatch et al. (1991) and Greatbatch and Xu (1993) show that a weakening of Gulf Stream throughout 1960's is traced to a change in JEBAR associated with bottom topography on the western side of the mid-Atlantic Ridge. Further study of the JEBAR effect associated with mid-Atlantic Ridge is necessary for the complete understanding of the response of the thermohaline structure to the decadal variation of the wind stress curl.

Although we have shown here that the observed thermohaline change in the North Atlantic was caused by the weakened wind stress curl, there is another possibility that the observed change was caused by the self-sustained oscillations of the oceanic circulation. This process is supported by the fact that the Bryan/Cox ocean general circulation models exhibit the interdecadal variability under the mixed boundary conditions (Weaver and Saratik, 1991). The thermohaline structure change demonstrated by these models, however, seems to be confined in the subpolar region, so that this process cannot explain the change in the thermohaline structure all over the North Atlantic, though it could be appropriate for the explanation of the thermohaline change in the subpolar gyre.

The numerical model used in this study resolves only two lowest vertical modes in the thermocline. Thus, we should discuss whether the generation mechanism of temperature variation presented in this study can apply for the continuously stratified ocean. The main horizontal features of mean temperature fields in the thermocline of the North Atlantic have been reproduced by two vertical modes in the thermocline. Therefore, we consider that two level representation of the thermocline is sufficient for investigating dynamics in the thermocline.

In the level model represented by lower vertical resolution, density structure depends

on the vertical grid spacing through the vertical density advection. Ikeda (1987) compared two level model represented by the centered difference with that represented by the up-stream difference, so that he showed that density structures were different between them. Therefore, it is worth examining the model which uses the up-stream difference in future, although our model has vertically four levels.

Our numerical model forms the mid-latitude closed system. The temperature distribution reproduced near the eastern and western boundaries is not correct because of the Kelvin wave propagation along the southern and northern boundaries. As mentioned in section 4.1, this effect leads to the disagreements between the model predicted temperature change and the observed one at both the subtropical eastern boundary and subpolar western boundary. The realistic model including all over the North Atlantic is needed to resolve this point.

# 7 Summary and conclusion

We have first discussed the thermohaline variability at intermediate depths of the North Atlantic throughout 1960's, and specified the following characteristic features of the observed variability:

1) The horizontal pattern of the thermohaline change shown by Levitus (1989) had the different tendencies between the western and eastern portions in both subtropical and subpolar gyers. The horizontal pattern of the thermohaline change geographically relates to the mean horizontal thermohaline structure at intermediate depths of the subtropical-subpolar system.

2) The observed change in the thermohaline structure mainly occurred in the thermocline.

3) The magnitude of the wind curl (hence, wind stress curl) over the North Atlantic subtropical-subpolar system decreased throughout 1960's.

Above observational evidences have yielded the following hypotheses:

1) The weakened wind stress curl over the North Atlantic caused the observed thermohaline change in the thermocline of the subtropical-subpolar system.
2) The thermohaline change due to a uniform change in the wind stress curl was different between the western and eastern portions, through dynamics in the ocean.

In order to test these hypotheses, a four-level model, which is driven by the wind stress and surface heat flux, has been constructed with thermohaline structures represented by a temperature field. The model has been used to examine responses of the subtropical-subpolar temperature field to a sudden and uniform change in the wind stress curl. The model has shown that the uniformly weakened wind stress curl generates the thermohaline change with different tendencies between the western and eastern domains in both subtropical and subpolar gyres, similar to the observed pattern.

Under the uniformly weakened wind stress curl, the thermohaline change with different tendencies between the western and eastern domains is not related to the linear theory (e.g., Anderson and Gill, 1975), which is based on the vertical shift of the thermocline caused by the Ekman pumping change and the long baroclinic Rossby wave propagation. In this study, the responses of the subtropical-subpolar temperature field have been related to the non-linear theory, which is based on the horizontal shift of the thermocline due to the advection effects in adding to its vertical shift. The model solutions have been analyzed using an analytical method: i.e., the characteristic curves associated with both a linear wave propagation and non-linear advection effects.

The major implications of the numerical experiment are as follows:

1) The spatial pattern of the horizontal temperature variation in the thermocline is principally related to two mechanisms; one is the formation of the temperature anomalies, and the other is the distribution of the temperature anomalies.

1-1) The formation mechanism of temperature anomalies is as follows: the vertical shift of the thermocline caused by the weakened wind stress curl results in the reduction of the velocity-structure-1 (similar to the 1st baroclinic mode), so that the change of the

horizontal heat advection forms temperature anomalies in the thermocline. The mean horizontal temperature structure in the thermocline, which is maintained by combined wind stress and surface buoyancy flux, plays an important role in forming temperature anomalies.

1-2) The temperature anomalies are distributed along the characteristics of the vertically integrated temperature in the thermocline(hence, heat content in the thermocline). The spatial pattern of characteristics which consist of the western and eastern domains is important to distribute temperature anomalies.

2) The thermal circulation is intensified by decrease in the magnitude of the wind stress curl. On the contrary, this circulation weakens by increase in the magnitude of the wind stress.

**Acknowledgments.** The author would like to thank Professor Sei-ichi Kanari, Professor Kensuke Takeuchi, Dr. Toshiyuki Hibiya, Dr. Shoshiro Minobe for their advice, and wish to acknowledge valuable discussions with Professor Motoyoshi Ikeda.

# References


[1] Anderson, D. L. T., and A. E. Gill, Spin-up of a stratified ocean, with applications, to upwelling, *Deep-Sea Res., 22*, 583-596, 1975.

[2] Anderson, D. L. T., and P. D. Killworth, Non-linear propagation of long Rossby waves, *Deep-Sea Res., 26*, 1033-1050, 1979.

[3] Bryan, K., A numerical method for the steady of the circulation of the world ocean, *J. Comput. Phys., 4*, 347-376, 1969.

[4] Bryan, K., and M. D. Cox, A nonlinear model of an ocean driven by wind and differential heating: Part I. Description of the three-dimensional velocity and density fields, *J. Atmos. Sci., 25*, 945-967, 1968.

[5] Colin de Verdiére, A., On the interaction of wind and buoyancy driven gyres, *J. Mar. Res., 47*, 595-633, 1989.

[6] Cushman-Roisin, B., On the maintenance of the subtropical front and its associated countercurrent, *J. Phys. Oceanogr., 14*, 1179-1190, 1984.

[7] Davey, M. K., A two-level model of a thermally forced ocean basin, *J. Phys. Oceanogr., 13*, 169-190, 1983.

[8] Dickson, R. R., J. Meincke, S.-A. Malinberg, and A. J. Lee, The great salinity anomaly in the northern North Atlantic, 1968-82, *Prog. Oceanogr., 20*, 103-151, 1988.

[9] Gill, A, E., and A. J. Clarke, Wind-induced upwelling, coastal currents and sea-level changes, *Deep-Sea Res., 21*, 325-345, 1974.

[10] Greatbatch, R. J., A. F. Fanning, A. G. Goulding, and S. Levitus, A diagnosis of interpentadal circulation changes in the North Atlantic, *J. Geophys. Res., 96(C12)*, 22,009-22,023, 1991.

[11] Greatbatch, R. J., and J. Xu, On the transport of volume and heat through sections across the North Atlantic: Climatology and the pentads 1955-1959, 1979-1974, *J. Geophys. Res., 98(C6)*, 10,125-10,143, 1993.

[12] Hellerman, S., and M. Rossenstein, Normal monthly wind stress over the world ocean with error estimations, *J. Phys. Oceangr., 13*, 1093-1104, 1983.

[13] Huang, R. X., A two-Level model for the wind-and buoyancy-forced circulation, *J. Phys. Oceanogr., 23*, 104-115, 1993.

[14] Ikeda, M., Wind effects on the buoyancy-driven general circulation in a closed basin using a two-level model, *J. Phys. Oceanogr., 17*, 1707-1723, 1987.

[15] Kushinir, Y., Interdecadal variation in the North Atlantic sea surface temperature and associated atmospheric conditions, *J. Climate, 5*, 141-156, 1994.

[16] Levitus, S., Climatological atlas of the world ocean, *NOAA Prof. Pap., 13*, Natl. Oceanic and Atmos., Washington, D. C., 1982.

[17] Levitus, S., Interpentadal variability of temperature and salinity at intermediate depths of the North Atlantic ocean, 1970-1974 versus 1955-1959, *J. Geophys. Res., 94*, 6091-6131, 1989.

[18] Liu, Z., Thermocline forced by varying Ekman pumping. Part I: spinup and spindown, *J. Phys. Oceanogr., 23*, 2505-2522, 1993a.

[19] Liu, Z., Thermocline forced by varying ekman pumping. Part II: annual and decadal Ekman pumping, *J. Phys. Oceanogr., 23*, 2523-2540, 1993b.

[20] Liu, Z., and J. Pedlosky, Thermocline forced by annual and decadal surface temperature variation, *J. Phys. Oceanogr., 24*, 587-608, 1994.

[21] Luyten, J. R., and H. Stommel, Gyres driven by combined wind and buoyancy flux, *J. Phys. Oceangr., 16*, 1551-1560, 1986.

[22] O'Brien, J, J., Oceanic interdecadal climate variability, *Intergovernmental Oceanographic Commission technical series., 40*, 1992.

[23] Roemmich, D., Sea level and the variability of the ocean, in glaciers, ice sheets, and sea level: Effect of a $CO_2$-induced climatic change, *DOE/ER/G0235-1*, pp. 104-115, Dep. of Energy, Washington, D. C., 1985.

[24] Talley, L. D., and M. E. Raymer, Eighteen-degree water variability, *J. Mar. Res., 40*, suppl. 1, 757-775, 1982.

[25] Weaver, A. J., E. S. Sarachik, and J. Marotzke, Freshwater flux forcing of decadal and interdecadal oceanic variability, *Nature, 353*, 836-838, 1991.

Table 1. Summary of parameter values used in this study.
$A_{MH}$: Lateral eddy viscosity, $A_{MV}$: Vertical eddy viscosity,
$A_{DH}$: Lateral eddy diffusivity, $A_{DV}$: Vertical eddy diffusivity.

| $A_{MH}$ ($cm^2/s$) | $A_{MV}$ ($cm^2/s$) | $A_{DH}$ ($cm^2/s$) | $A_{DV}$ ($cm^2/s$) |
|---|---|---|---|
| $2\times10^8$ | 1.5 | $5\times10^6$ | 1.0 |

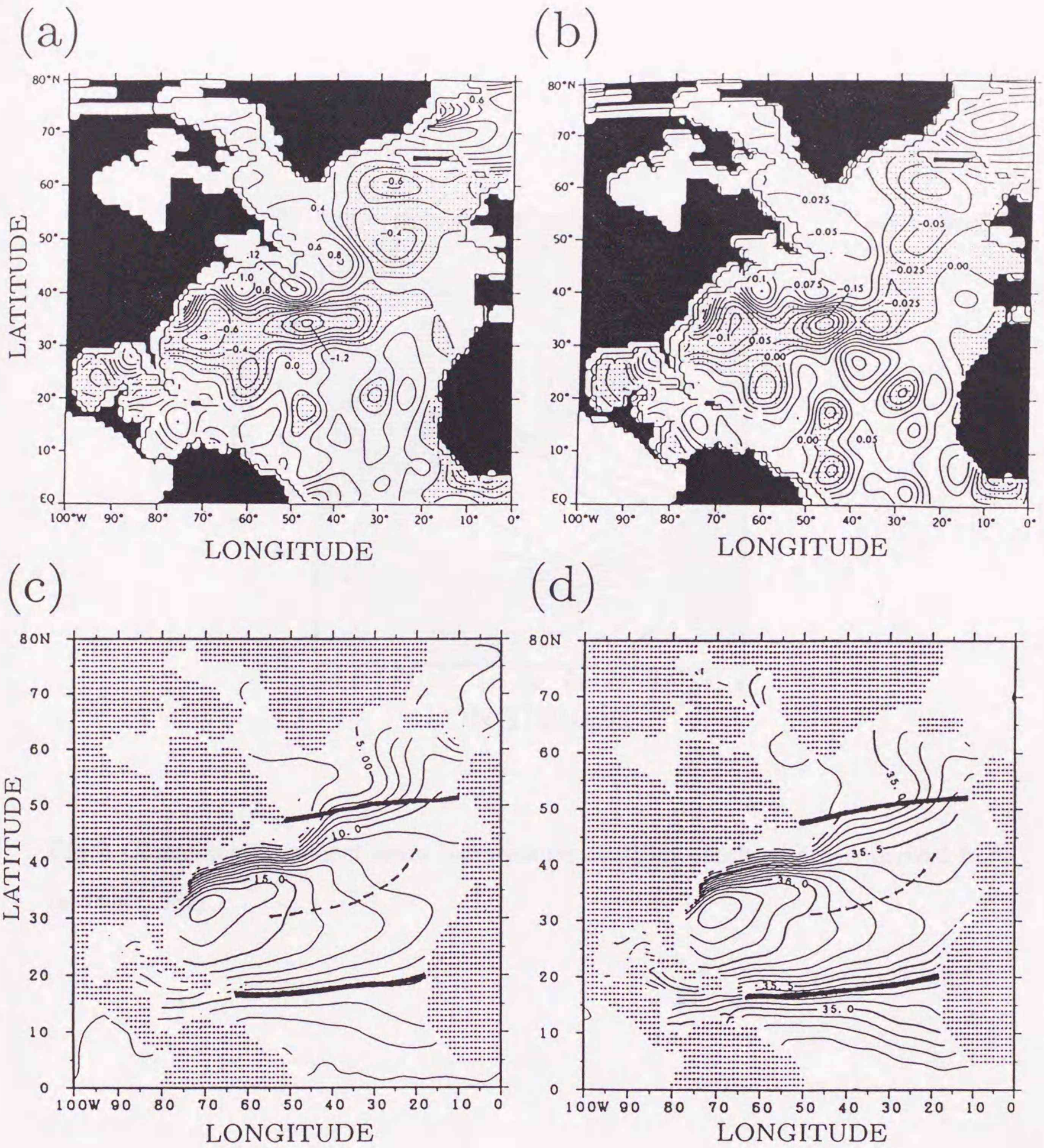


**Fig.1** (a) Temperature difference (in degrees Celsius) and (b) salinity difference (per mil) for 1970-1974 minus 1955-1959 at 500m depth from Levitus (1989). Dot shading indicates negative values. (c) Climatological annual mean temperature and (d) salinity at 500m depth, which are derived from Levitus (1982). Bold lines in (c) and (d) indicate gyre boundaries identified by zero lines of the Sverdrup transport stream function.

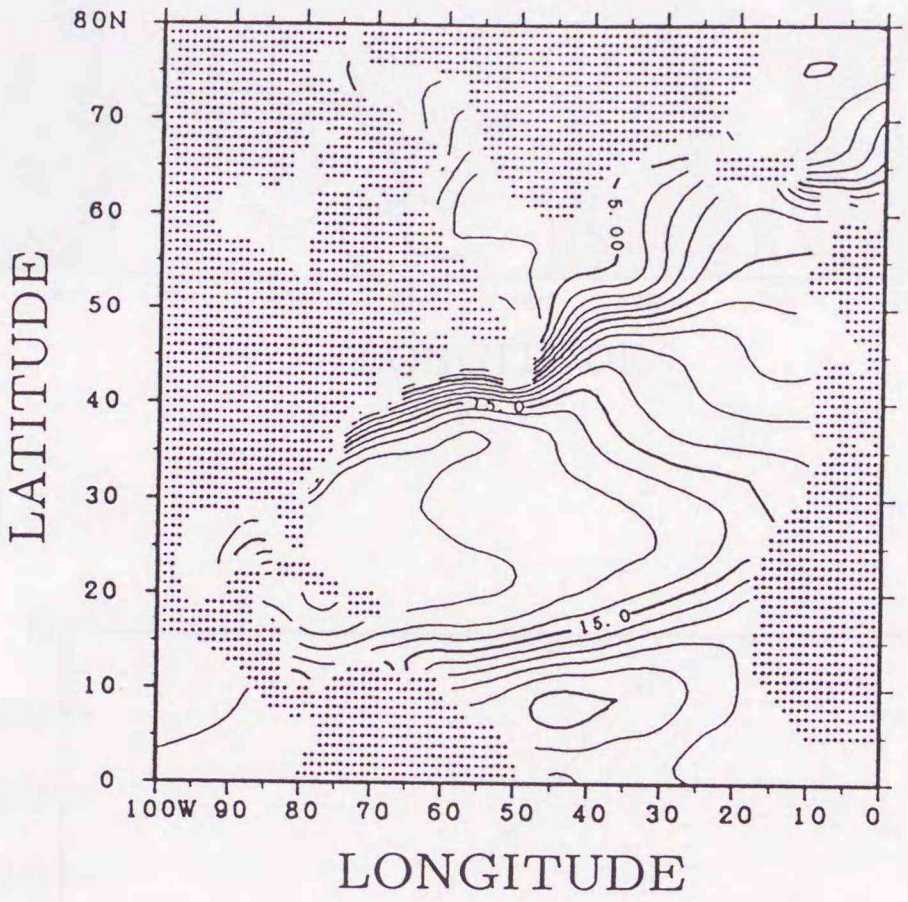


**Fig.2** Climatological annual mean temperature at 250m depth, which is derived from Levitus (1982).

(a)

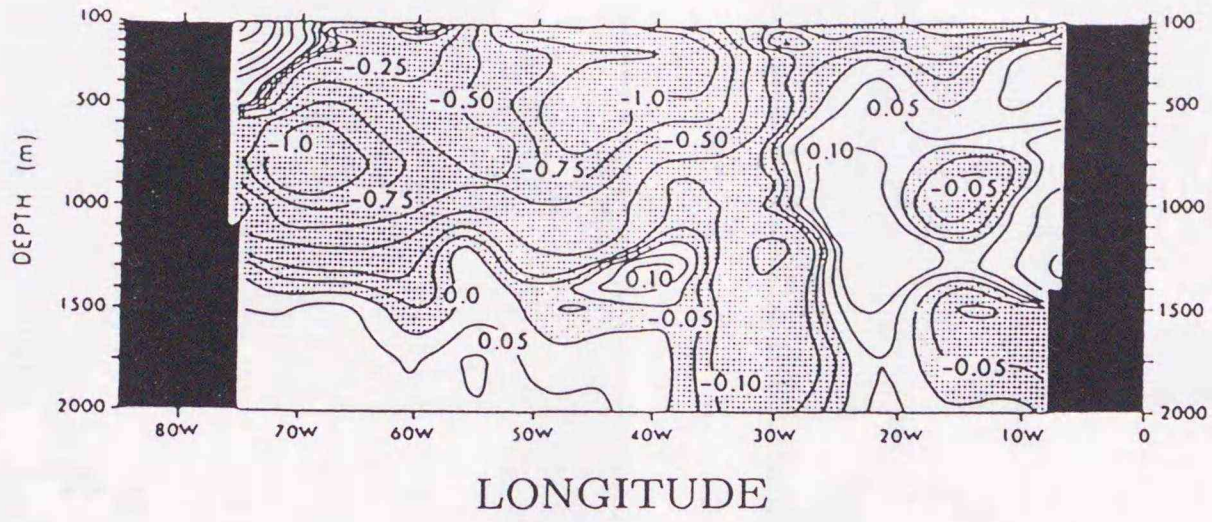


(b)

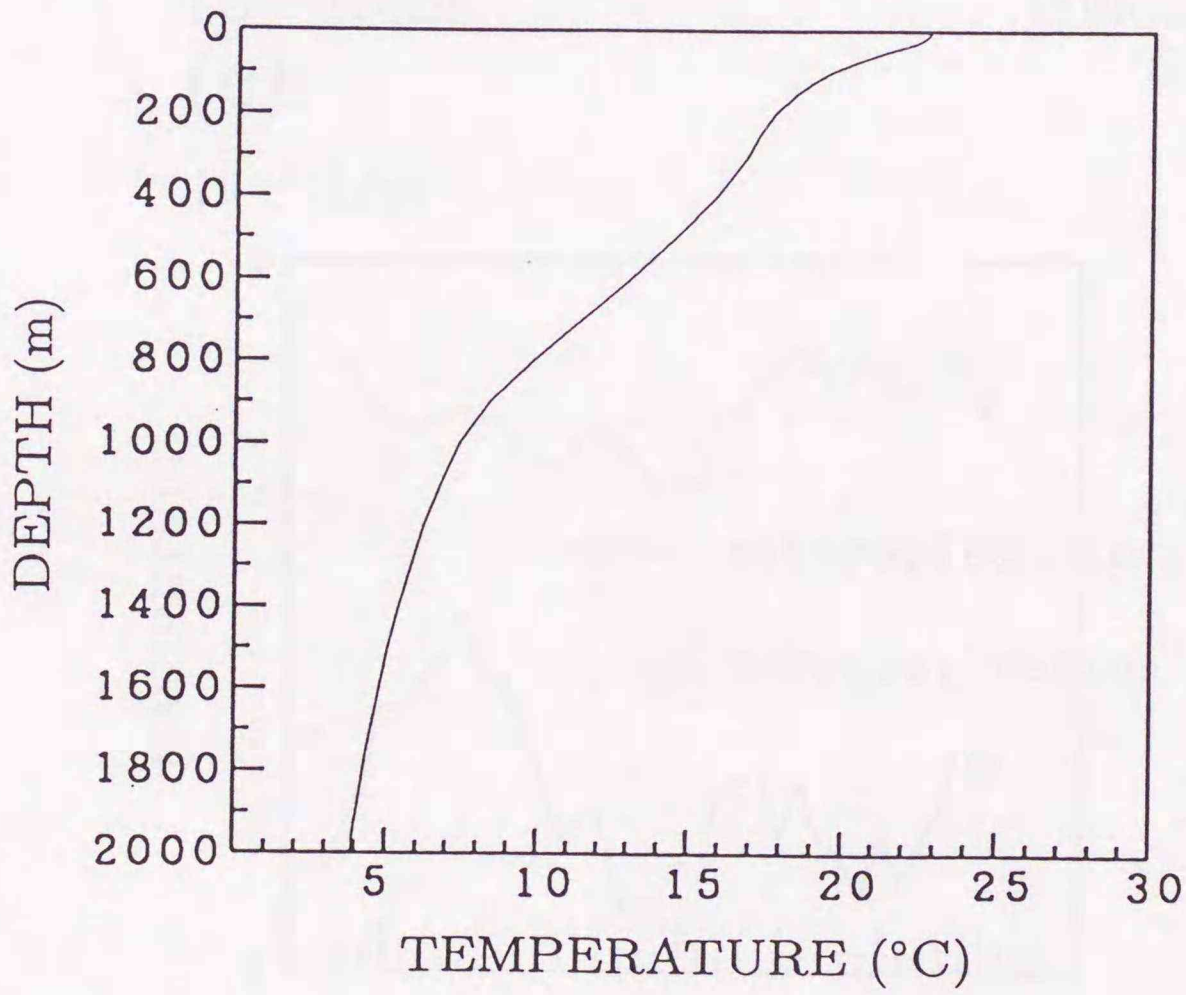


**Fig.3** (a) Temperature difference (in degrees Celsius) versus depth along 34.5°N in the North Atlantic for 1970-1974 minus 1955-1959 from Levitus (1989). Dot shading indicates negative values. (b) Climatological annual mean vertical temperature profile averaged along 30°N in the North Atlantic, which is derived from Levitus (1982).

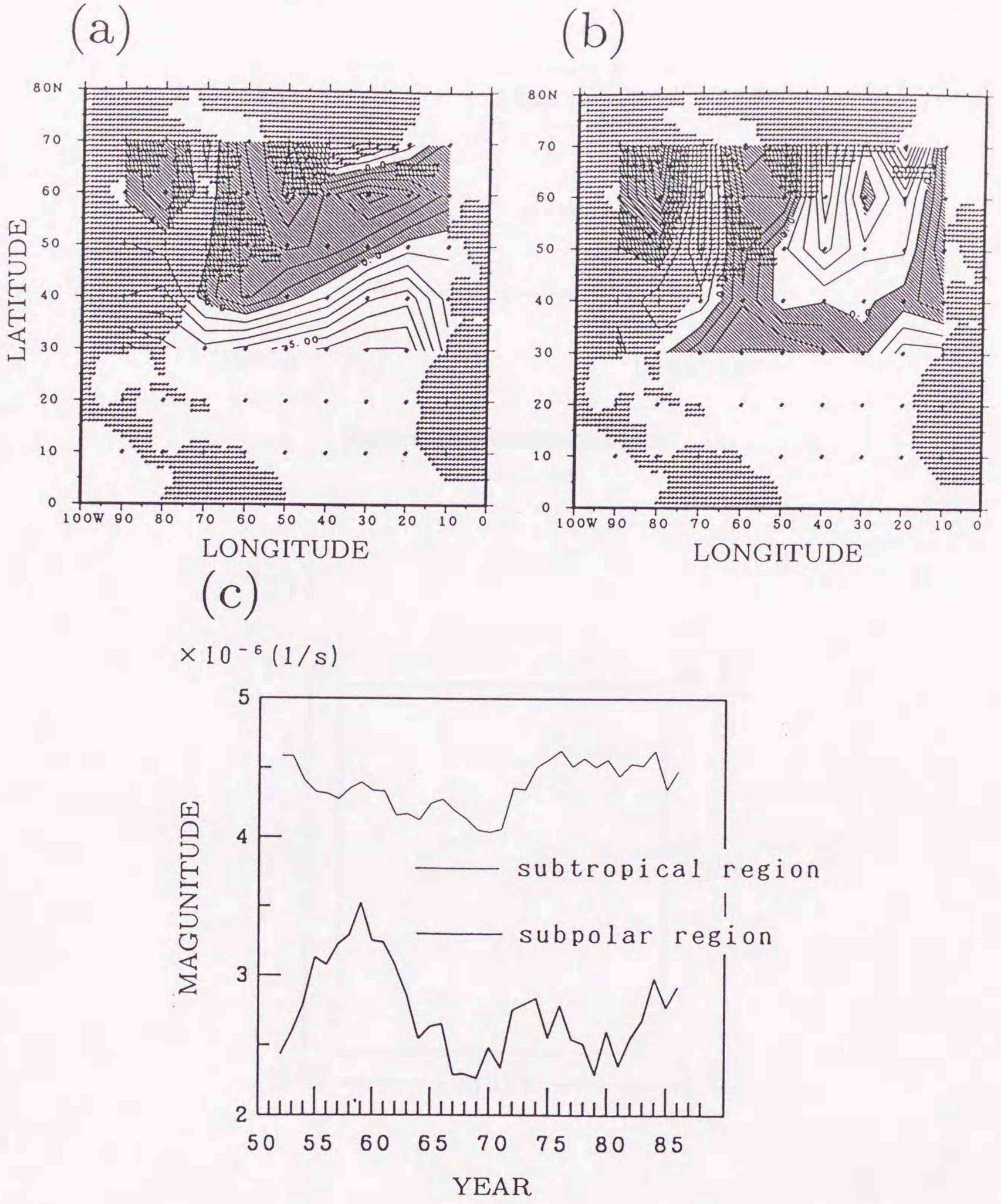


**Fig.4** (a) Climatological annual mean wind curl averaged during 1952-1988 period. (b) Wind curl difference for 1970 minus 1955. Hatched areas in (a) and (b) indicate negative values. Contour intervals in (a) and (b) are $1\times10^{-6}$ $s^{-1}$. (c) Time series of the magnitude (absolute value) in the wind curl which is averaged over each subtropical and subpolar gyre. These show 5-year running mean values.

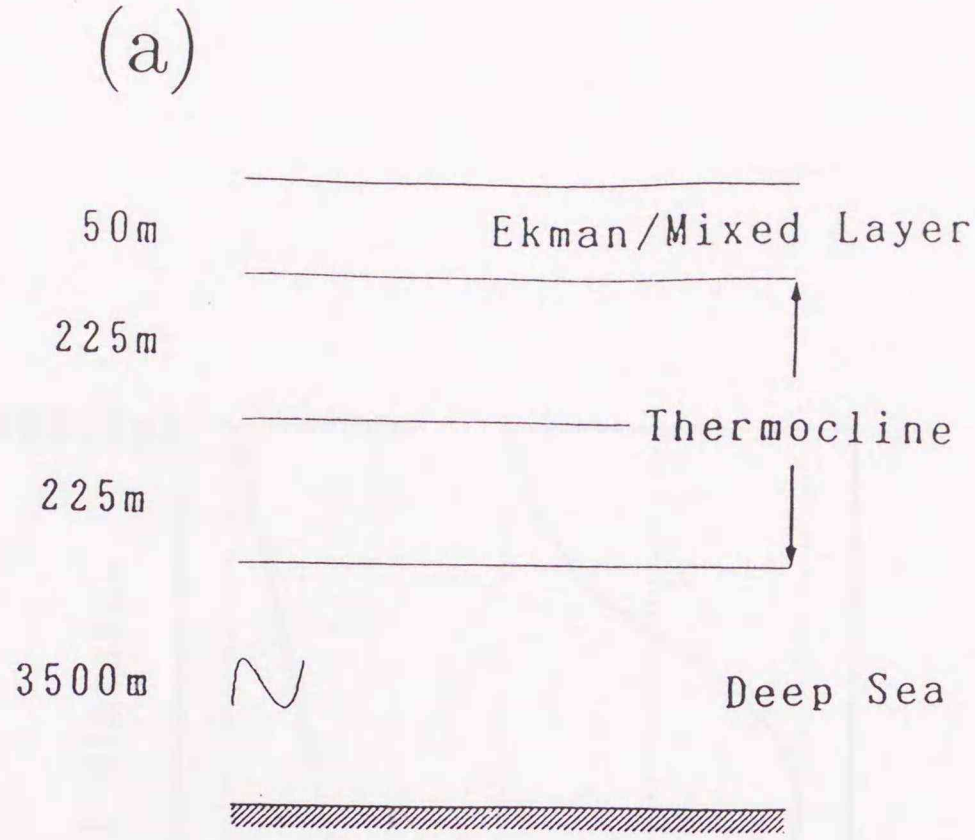


**Fig.5** Four level geometry: (a) vertical section showing depths, and (b) horizontal plan of the basin.

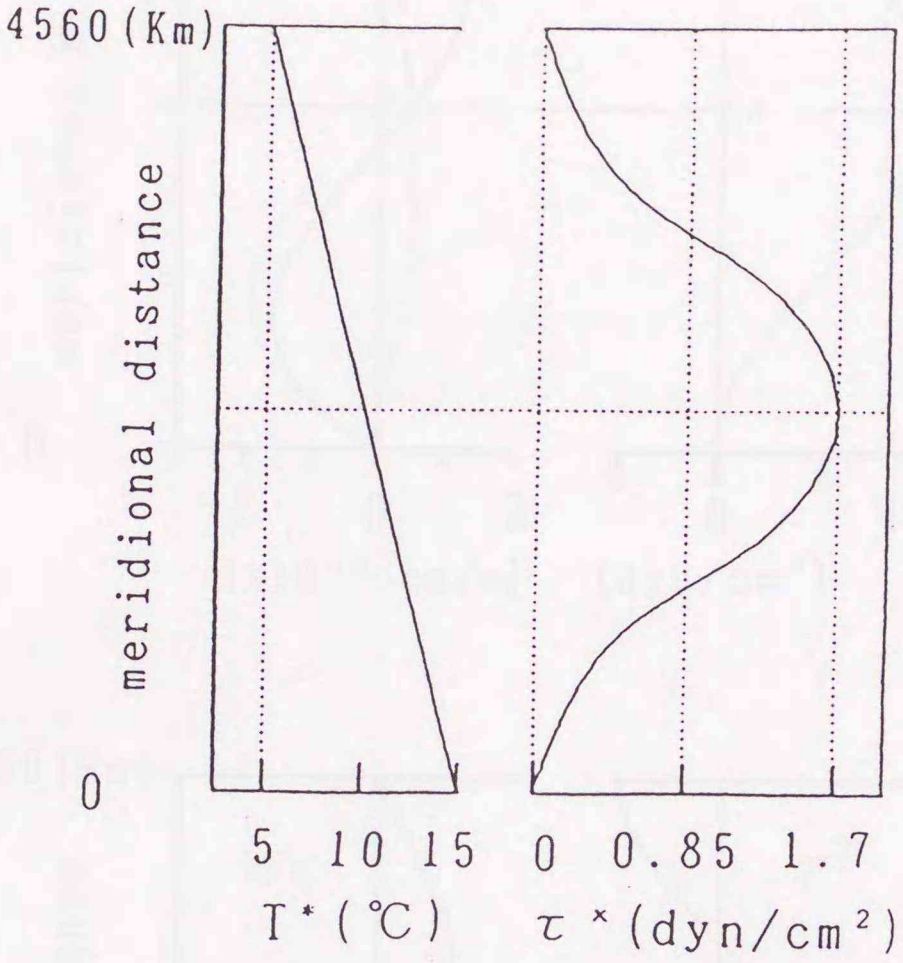


**Fig.6** Zonal wind stress and reference temperature at the surface.

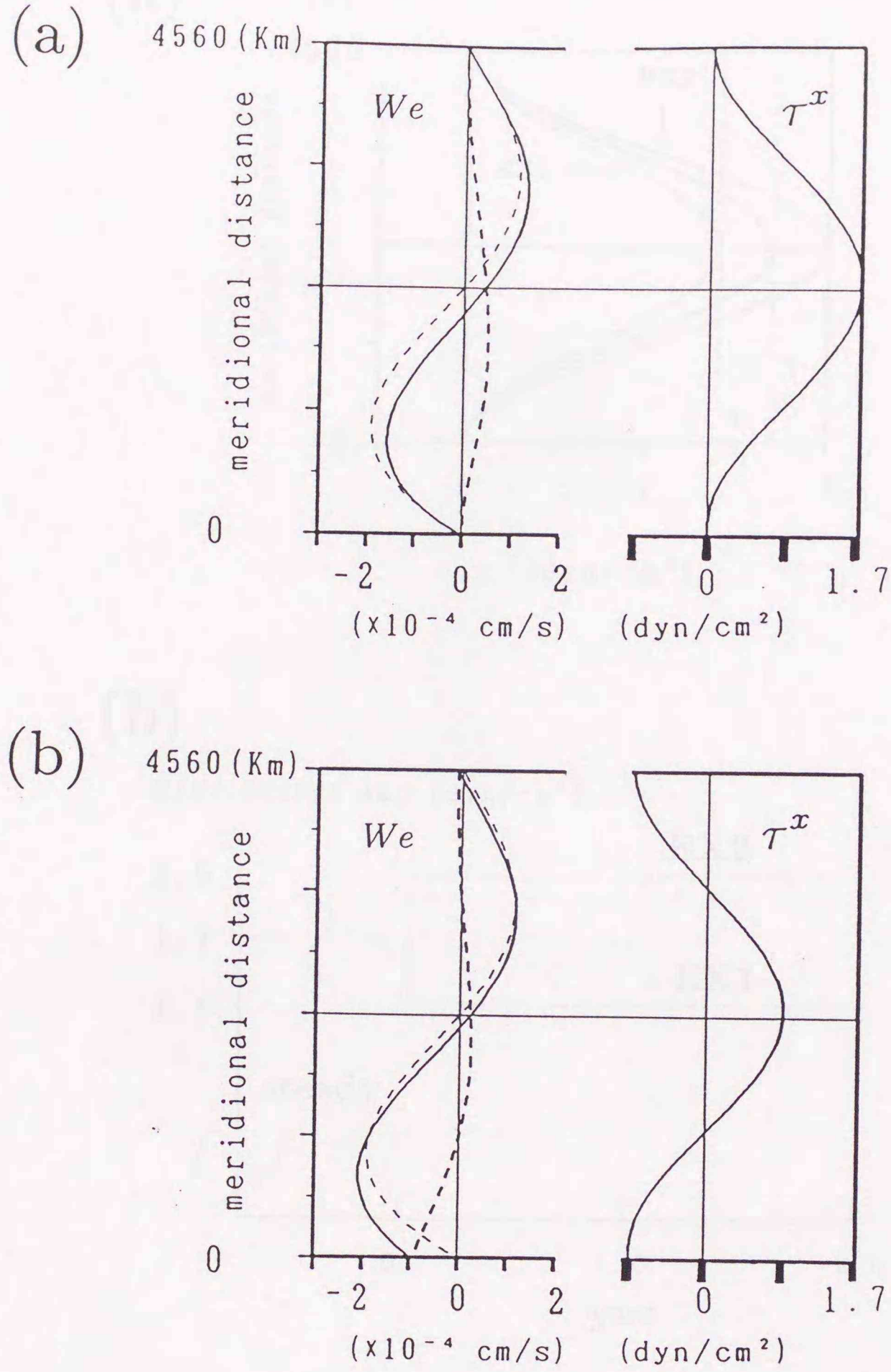


**Fig.7** Zonal wind stress; $\tau^x$, and Ekman pumping; $We = -1/f(\partial\tau^x/\partial y) + \beta/f^2(\tau^x)$, (a) in this study and (b) in most of the previous theoretical studies. Bold solid line indicates $We$, dashed line $-1/f(\partial\tau^x/\partial y)$, and bold dashed line $\beta/f^2(\tau^x)$ on the left side of each figure.

(a)

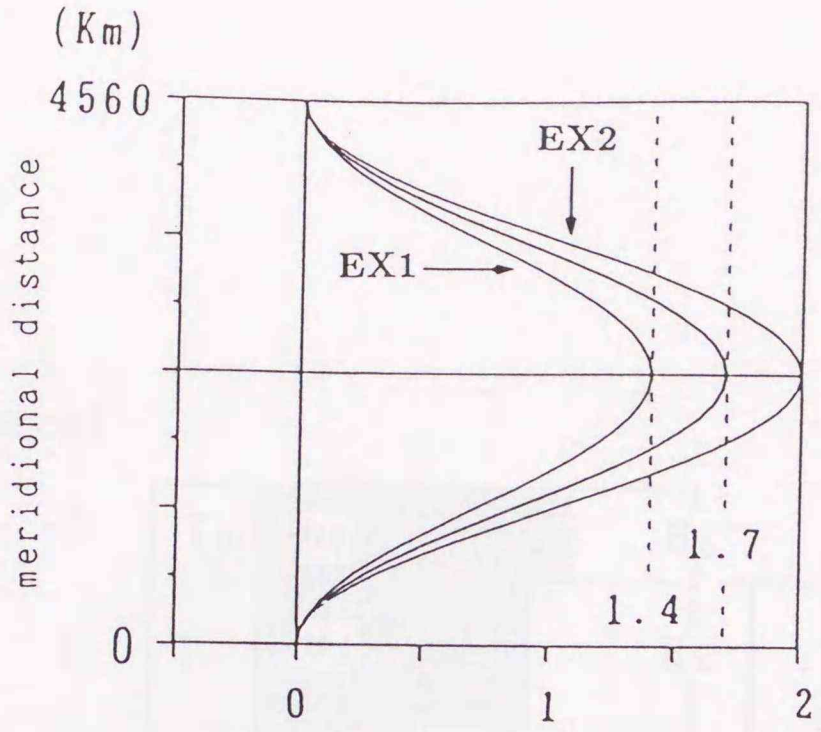


(b)

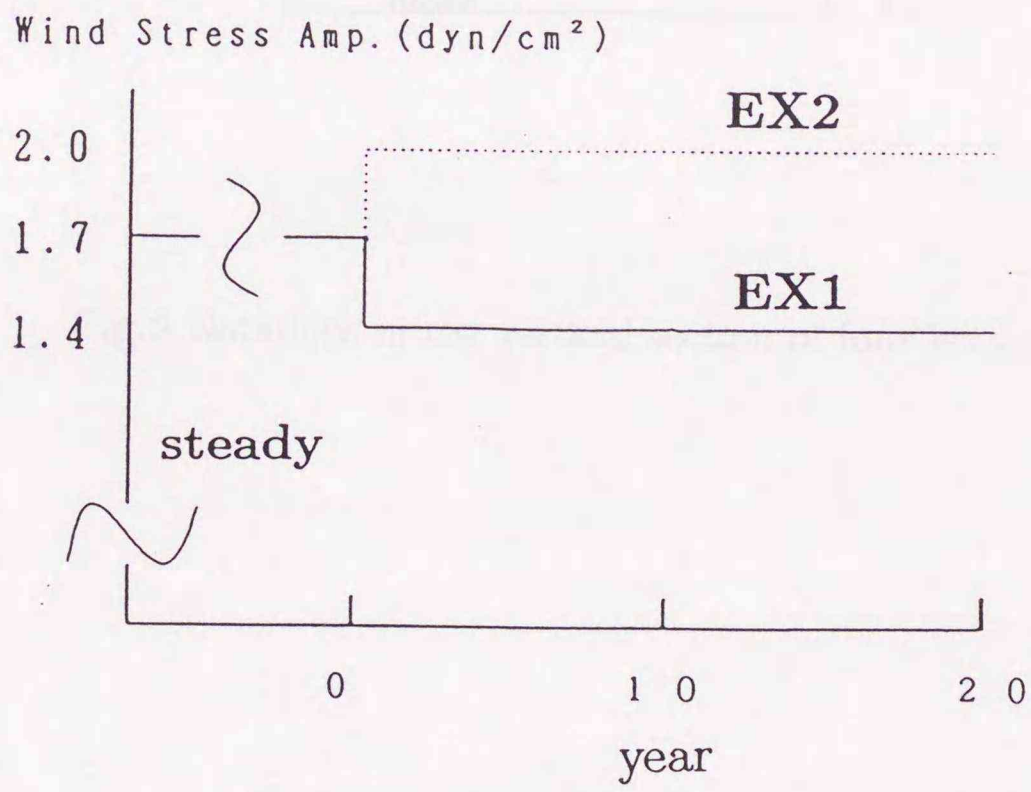


**Fig.8** (a) Spatial and (b) temporal changes in the zonal wind stress for Experiment 1 (EX1) and Experiment 2 (EX2).

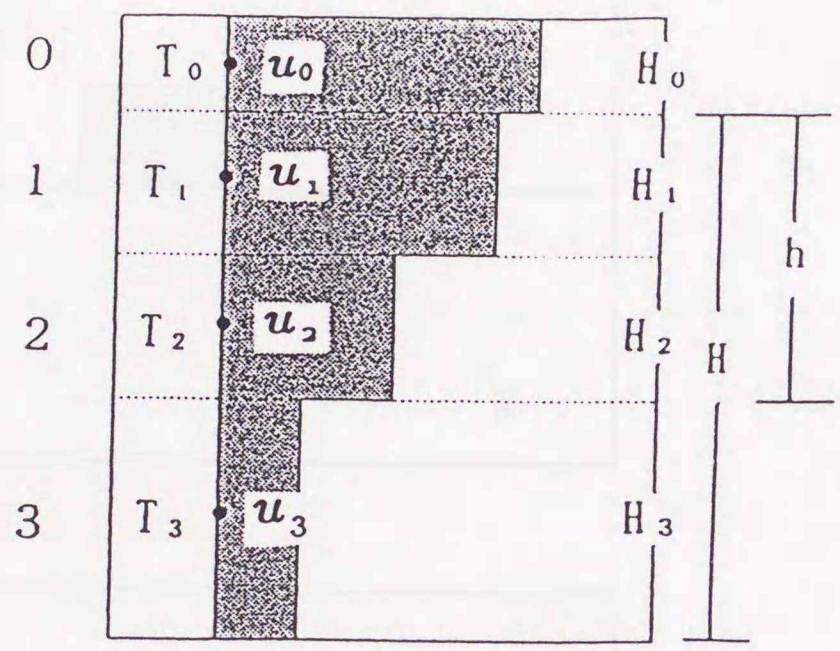


**Fig.9** Notations in the vertical section of four level model.

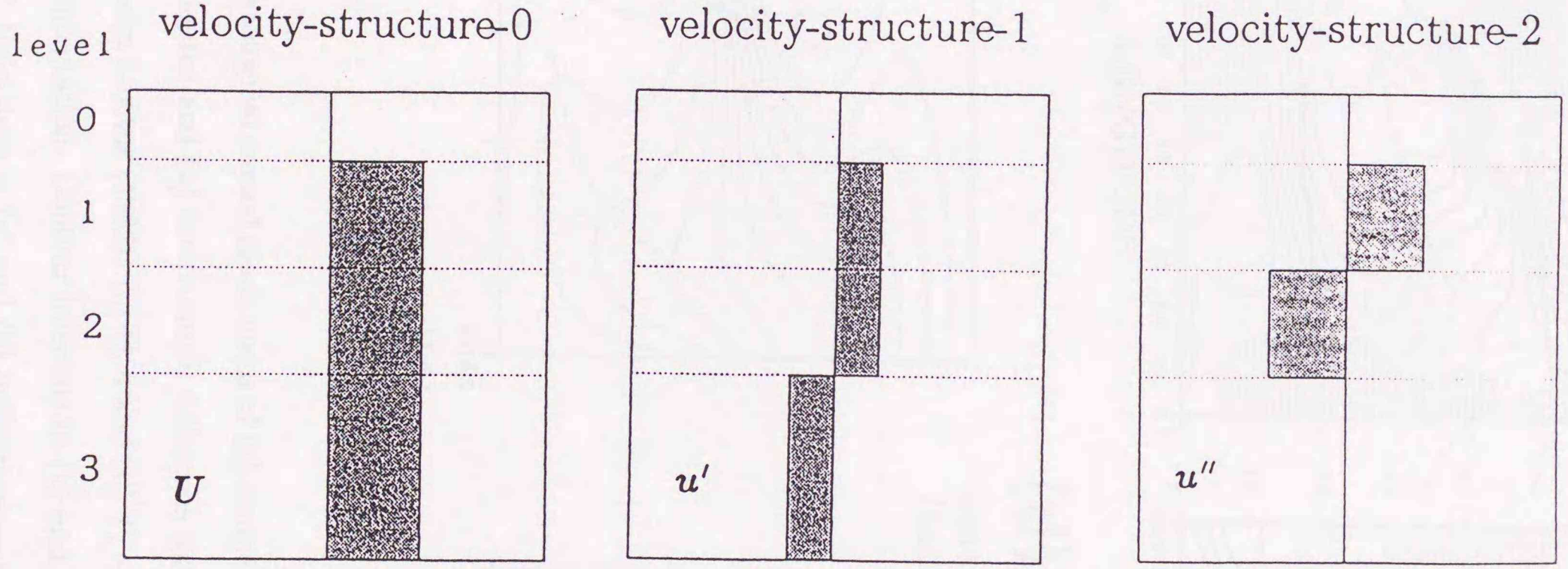


**Fig.10** Schematic view of the velocity-structure-0, 1 and 2.

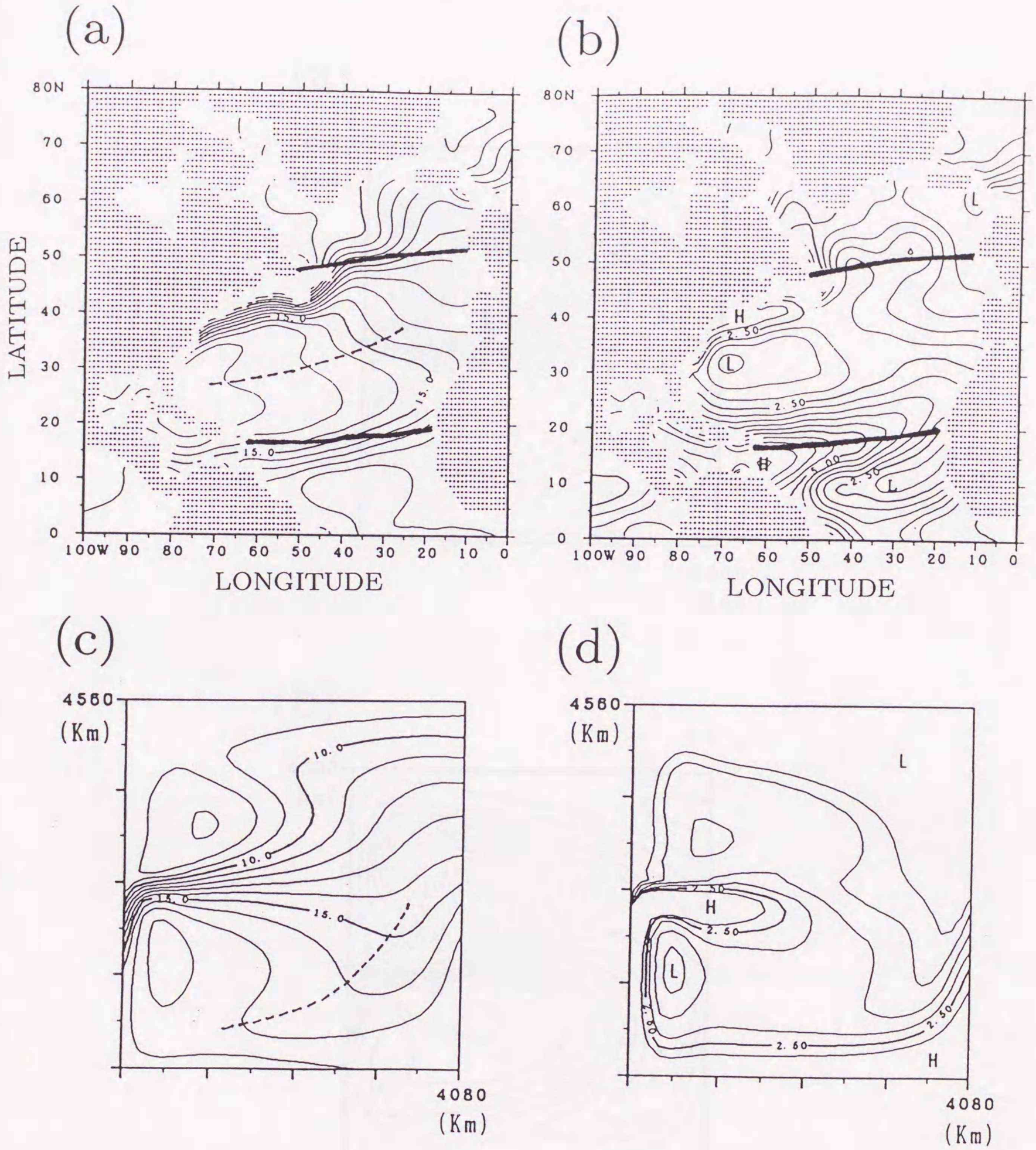


**Fig.11** Climatological annual mean maps of (a) temperature averaged vertically between 100m-500m depths and (b) temperature difference for 200m minus 400m depth. These are derived from Levitus (1982). (c) $\Theta/h$ and (d) $T_1 - T_2$ in the steady state quoted for 400 years of integration. Contour intervals in (a) and (c) are 1°C, and these in (b) and (d) are 0.5°C. Bold lines in (a) and (b) indicate gyre boundaries identified by zero lines of the Sverdrup transport stream function.

(a)

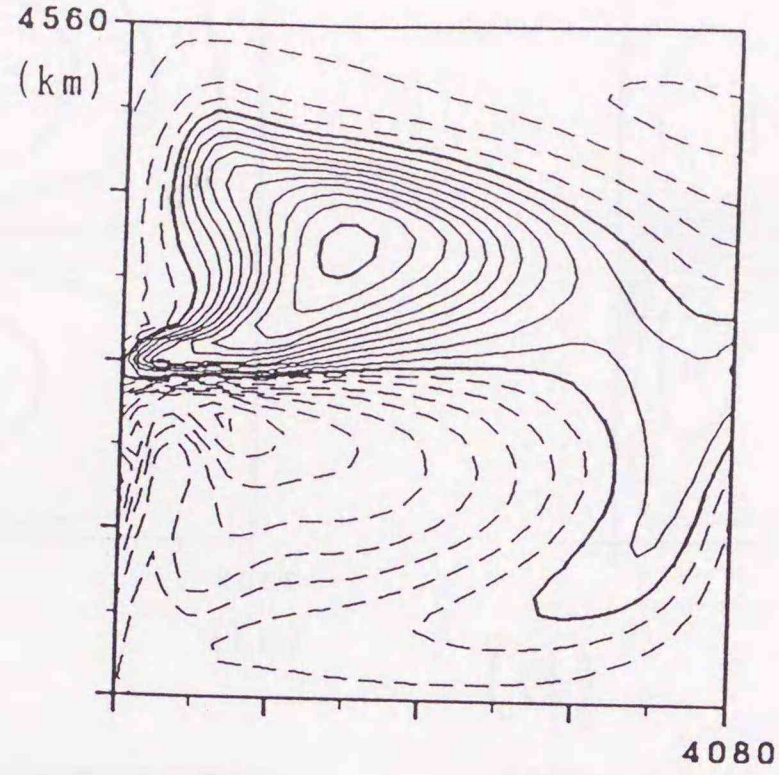


(b)

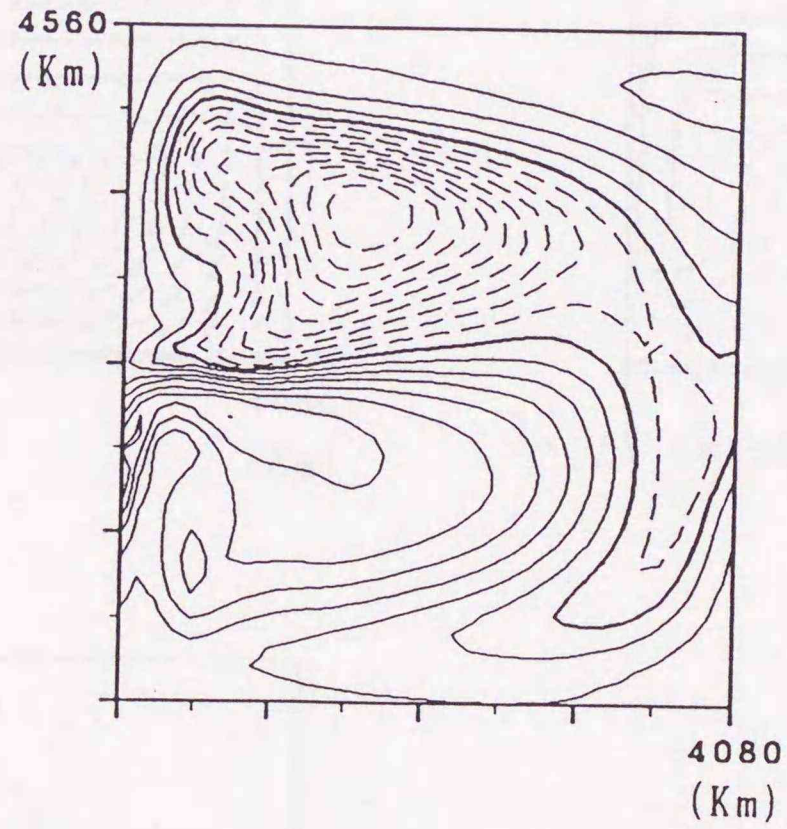


**Fig.12** Differences of $\Theta/h$ for 20-year minus 0-year in (a) EX1 and (b) EX2. Dashed lines indicate negative values. Contour interval is 0.1°C.

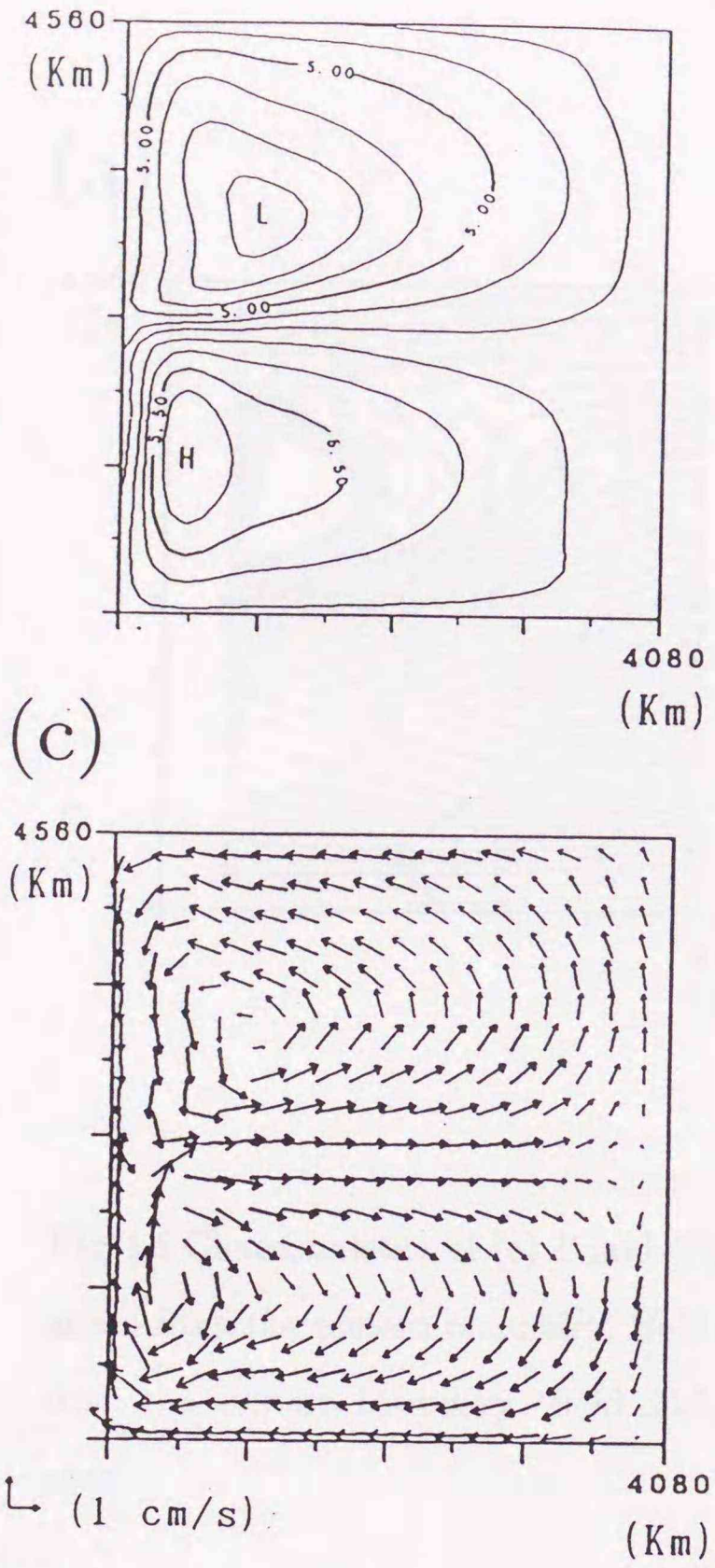


**Fig.13** (a) $\Gamma/H$, (b) $\Theta/h$, (c) velocity-structure-1 ($\boldsymbol{u}'$), (d) velocity-structure-2 ($\boldsymbol{u}''$) and (e) stream function in the steady state. Bold arrows in (c) and (d) show velocity more than 1cm/s. Contour interval in (e) is 5 Sv($10^6$ $m^3s^{-1}$).

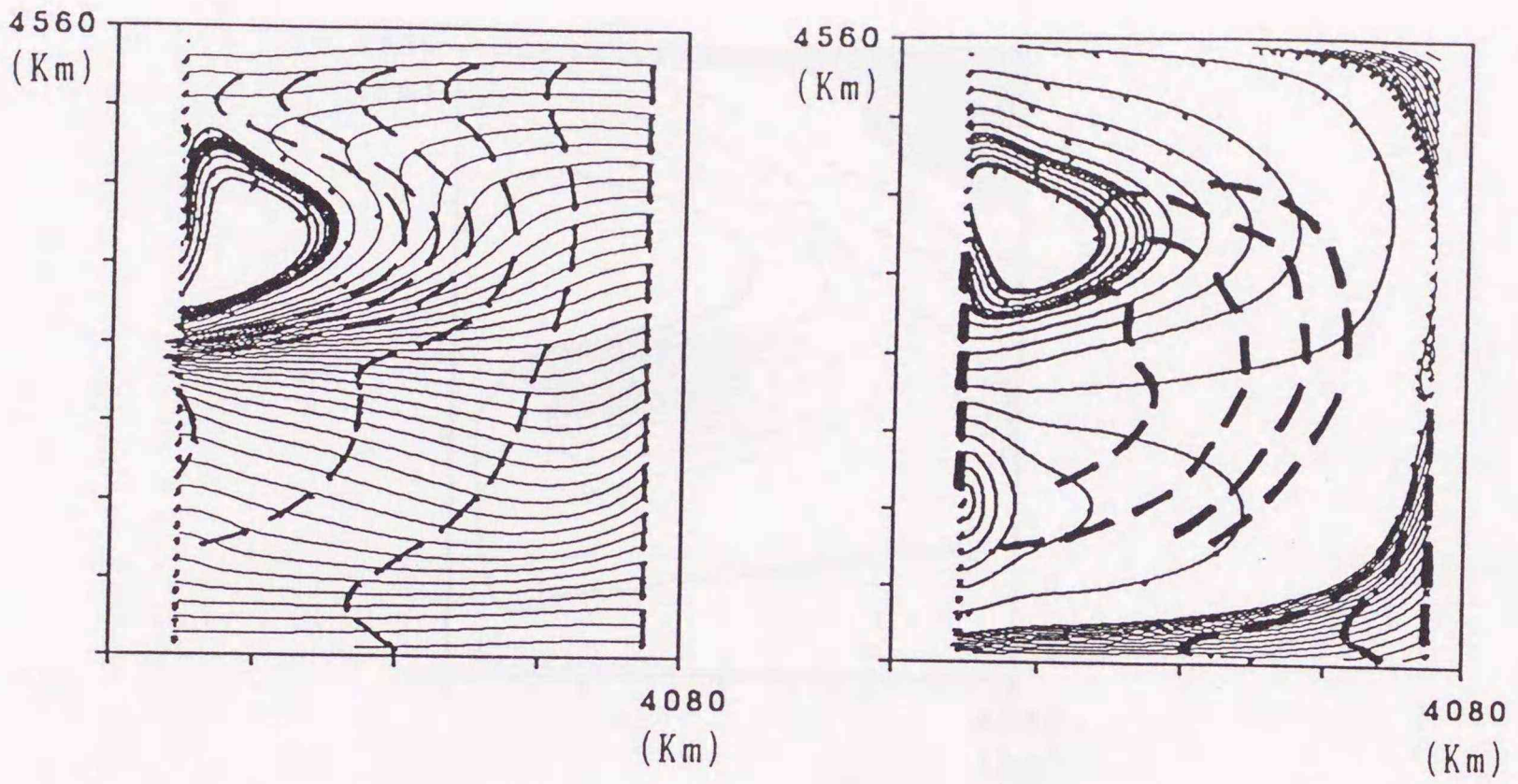


**Fig.14** Characteristics of (a) $\Gamma$ and (b) $\Theta$. Solid lines indicate characteristics which emanate from the eastern boundary. Bold solid lines indicate characteristics which emanate from the western boundary. Bold dashed lines indicate fronts which advance every one year.

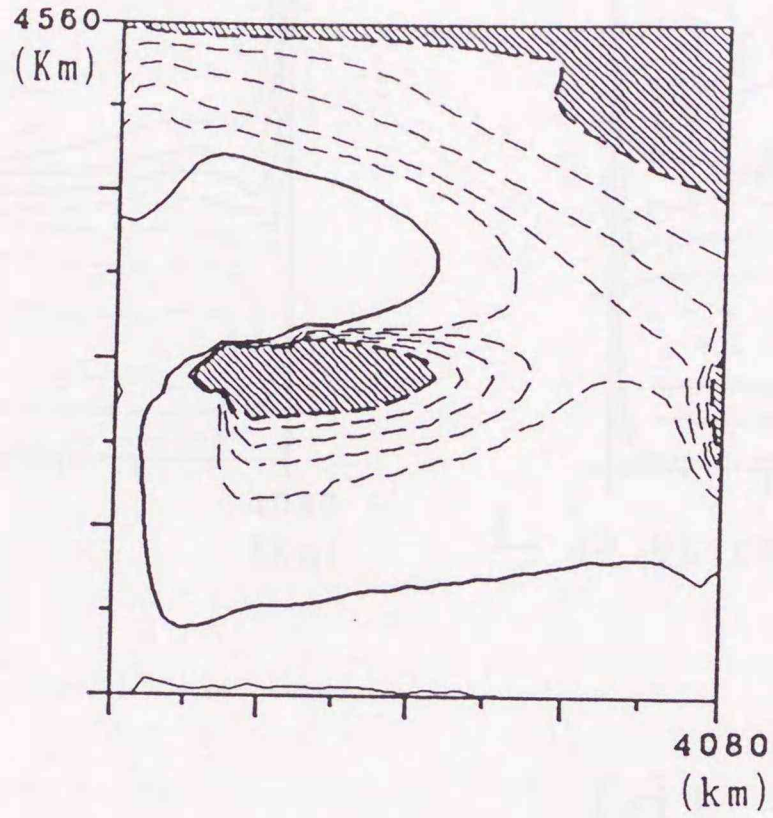


**Fig.15** Convection term in (4.1.26) or (4.1.27) in the steady state. Dashed line indicates negative value. Contour interval is $2 \times 10^{-4}$ °C cm $s^{-1}$. Hatched areas indicate active convection regions.

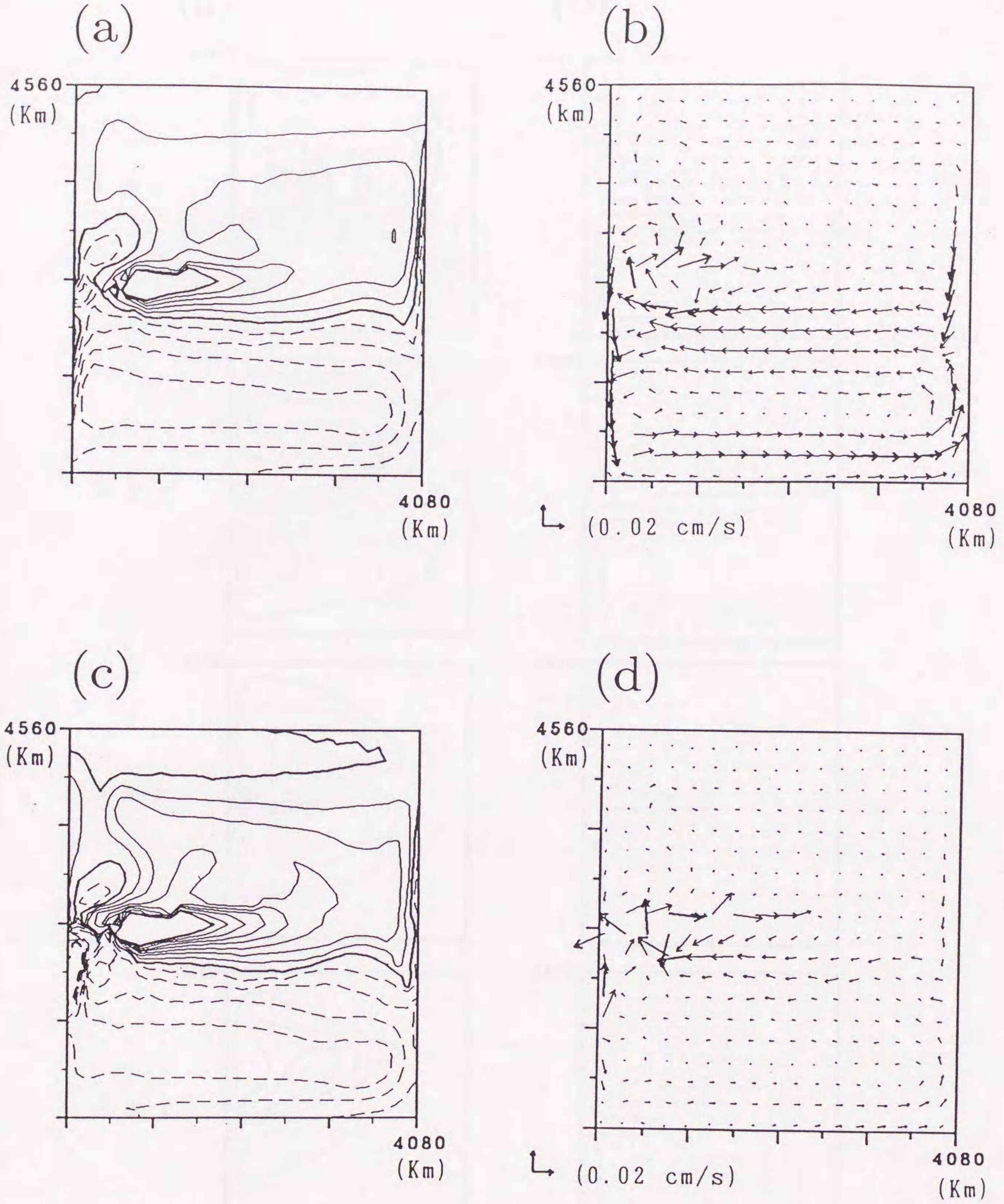


**Fig.16** Differences of (a) $\Gamma/H$, (b) velocity-structure-1, (c) $\Theta/h$ and (d) velocity-structure-2 for 30-day minus 0-day. Dashed lines in (a) and (c) indicate negative values. Contour intervals in (a) and (c) are $5 \times 10^{-3}$ °C and $2.5 \times 10^{-2}$ °C, respectively. Bold arrows in (b) and (d) show velocity difference more than 0.03cm/s.

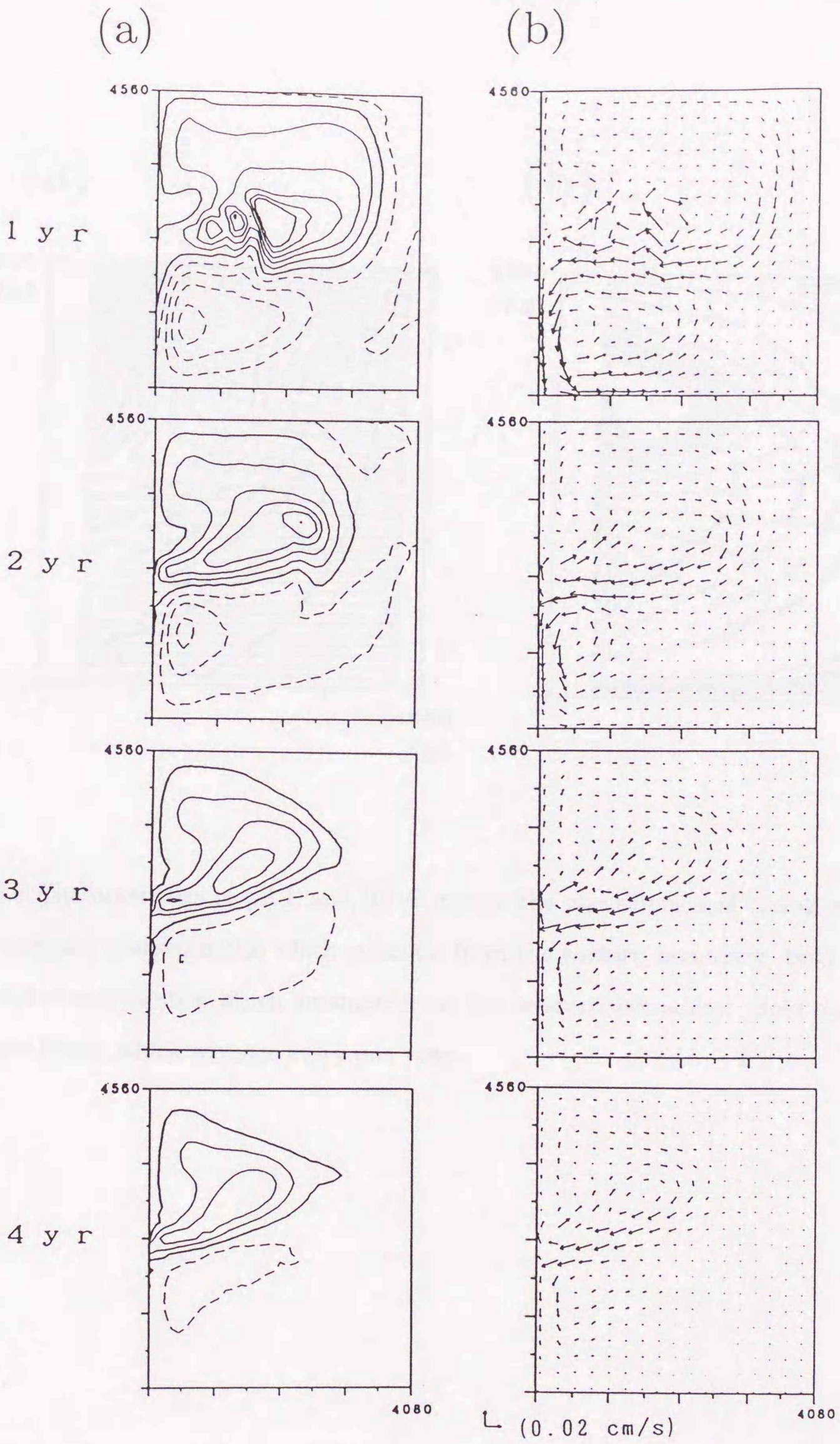


**Fig.17** Time series of (a) $\Gamma/H$ anomaly and (b) velocity-structure-1($\boldsymbol{u}'$) anomaly from 0-year to 4-year. These anomalies show the difference for every one month. Dashed line in (a) indicates negative value. Contour interval in (a) is $5 \times 10^{-3}$ °C. Bold arrow in (b) shows velocity difference more than 0.03cm/s.

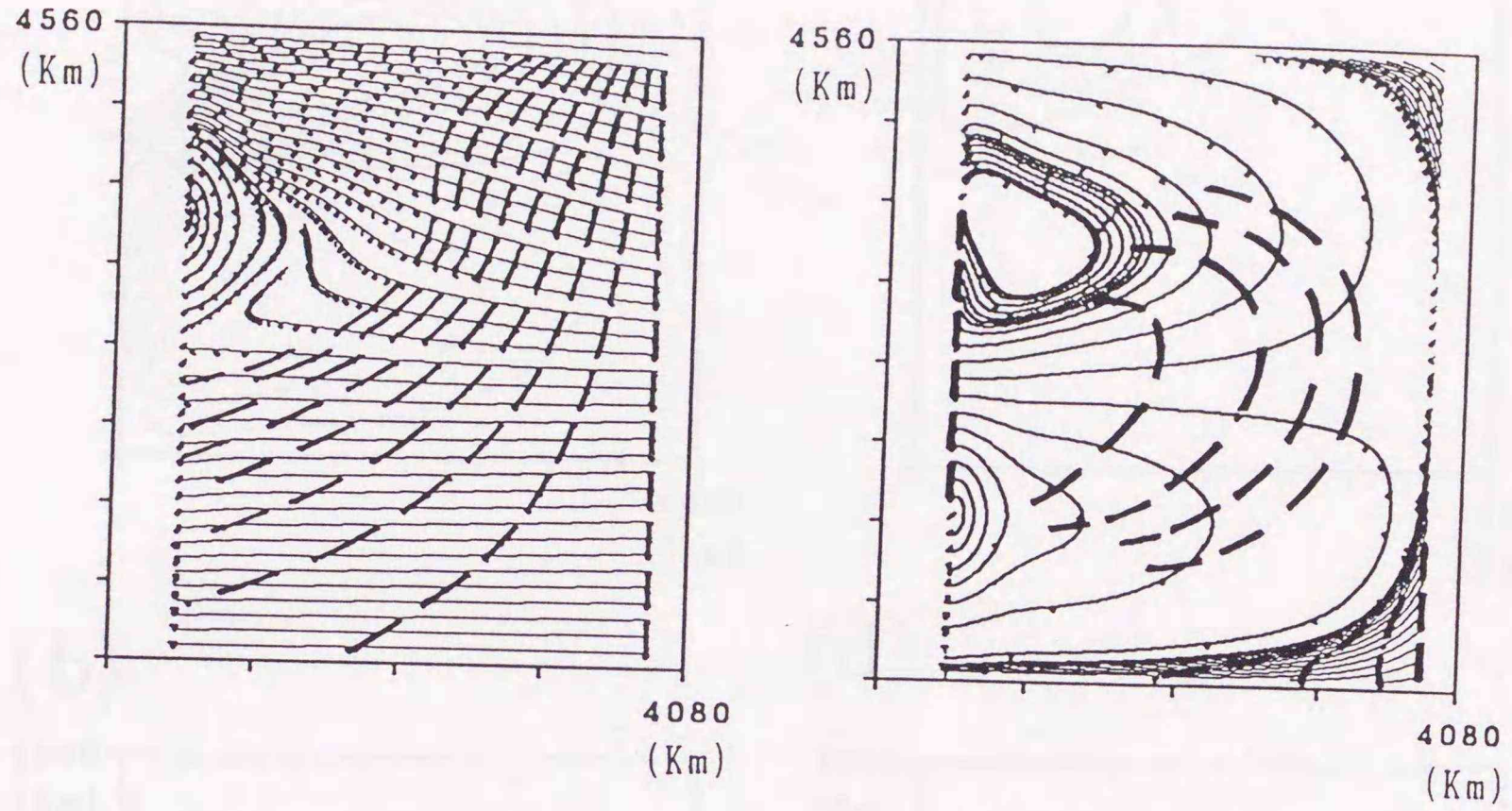


**Fig.18** Characteristics of (a) $\Gamma$ and (b) $\Theta$ except the contribution of type-2 wave. Solid lines indicate characteristics which emanate from the eastern boundary. Bold solid lines indicate characteristics which emanate from the western boundary. Bold dashed lines indicate fronts which advance every one year.

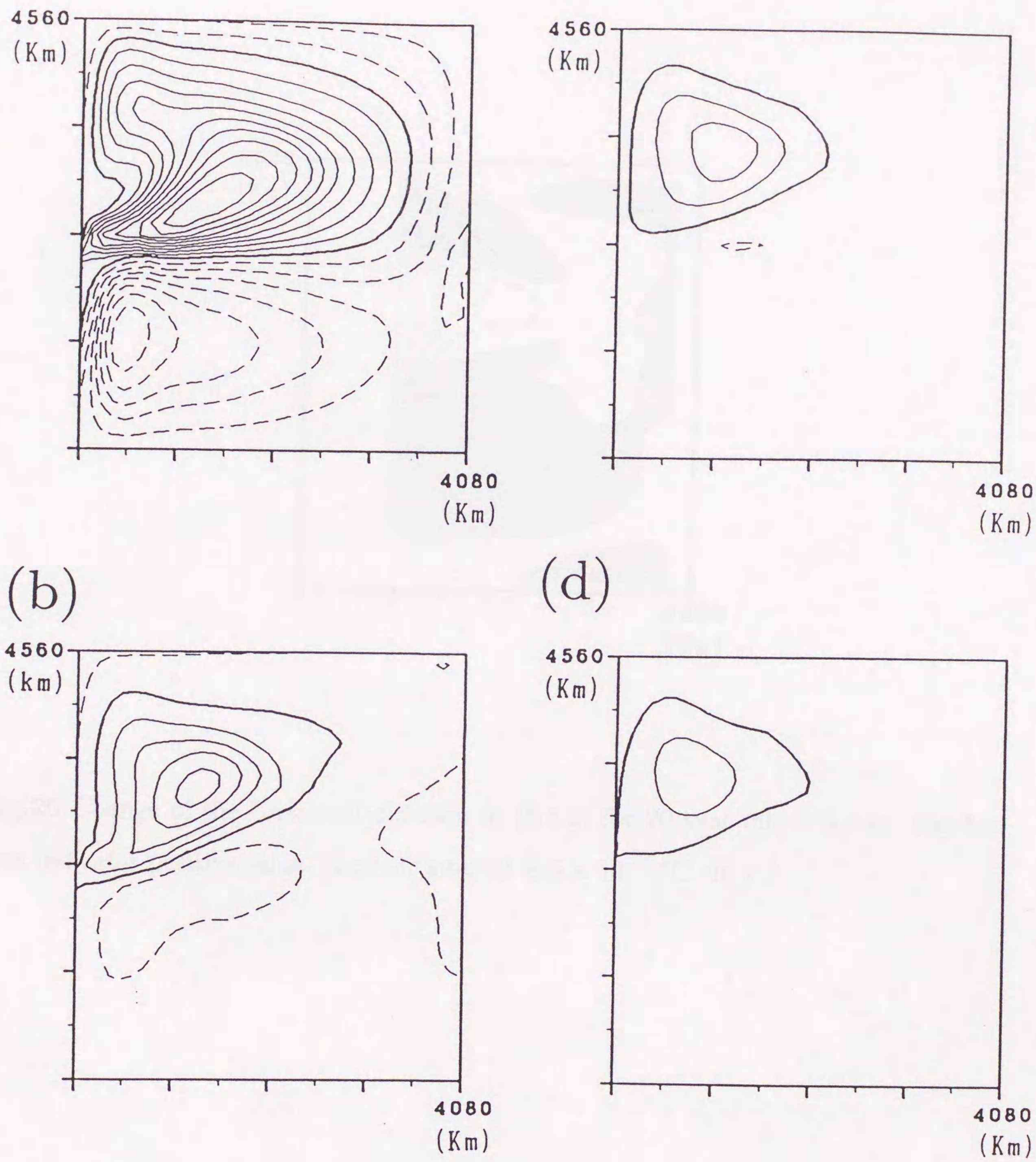


**Fig.19** Differences of $\Gamma/H$ for (a) 5-yr minus 0-yr, (b) 10-yr minus 5-yr, (c) 15-yr minus 5-yr and (d) 20-yr minus 15-yr. Dashed lines indicate negative values. Contour interval is 0.01°C.

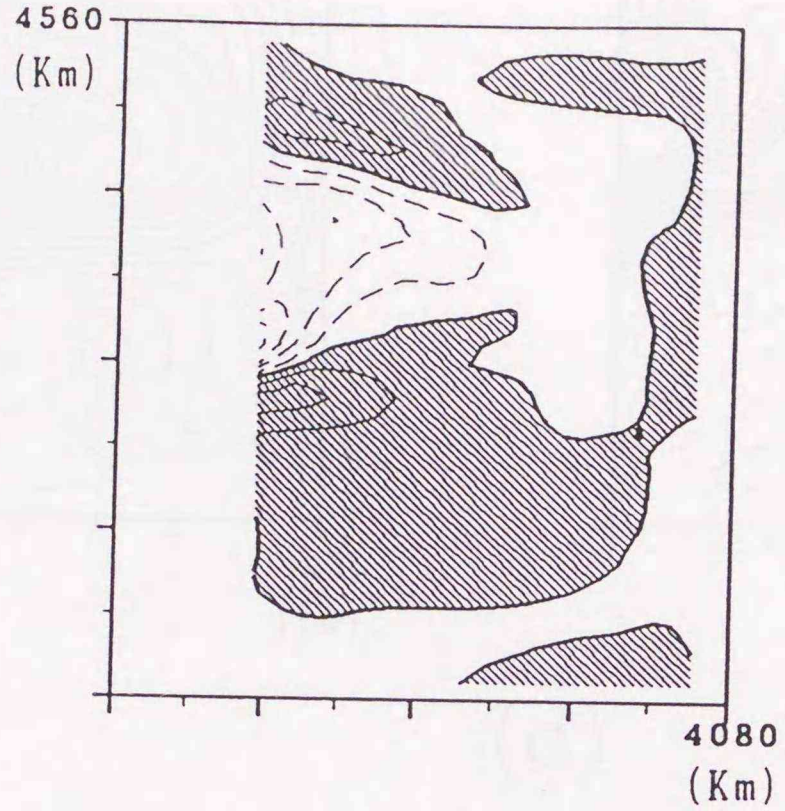


**Fig.20** Change of the horizontal diffusion in (5.4.2) for 20-year minus 0-year. Hatched area indicates positive value. Contour interval is $5 \times 10^{-5}$ °C cm $s^{-1}$.

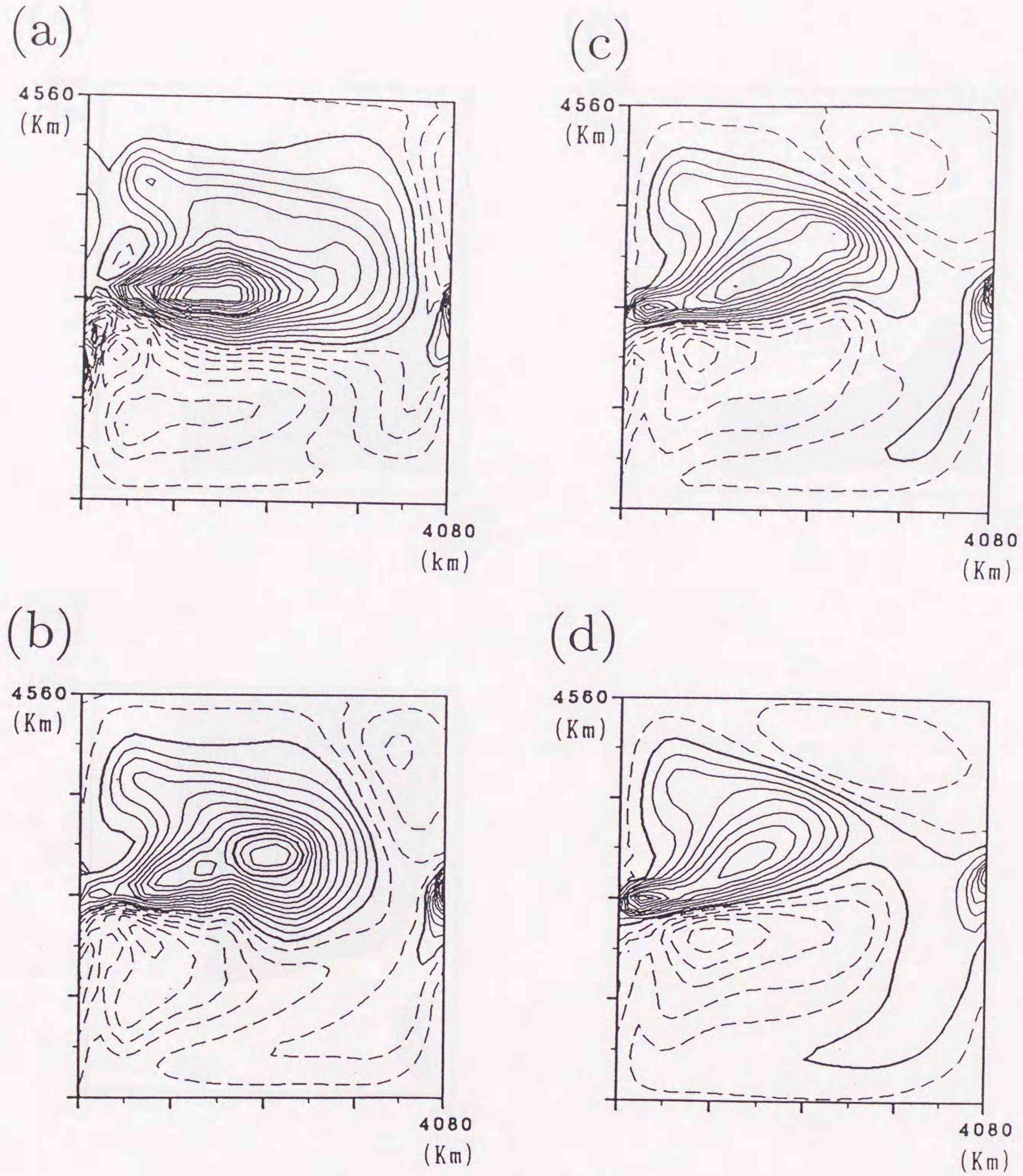


**Fig.21** Differences of $\Theta/h$ for (a) 1-yr minus 0-yr, (b) 2-yr minus 1-yr, (c) 3-yr minus 2-yr and (d) 4-yr minus 3-yr. Dashed line indicates negative value. Contour interval is 0.02°C.

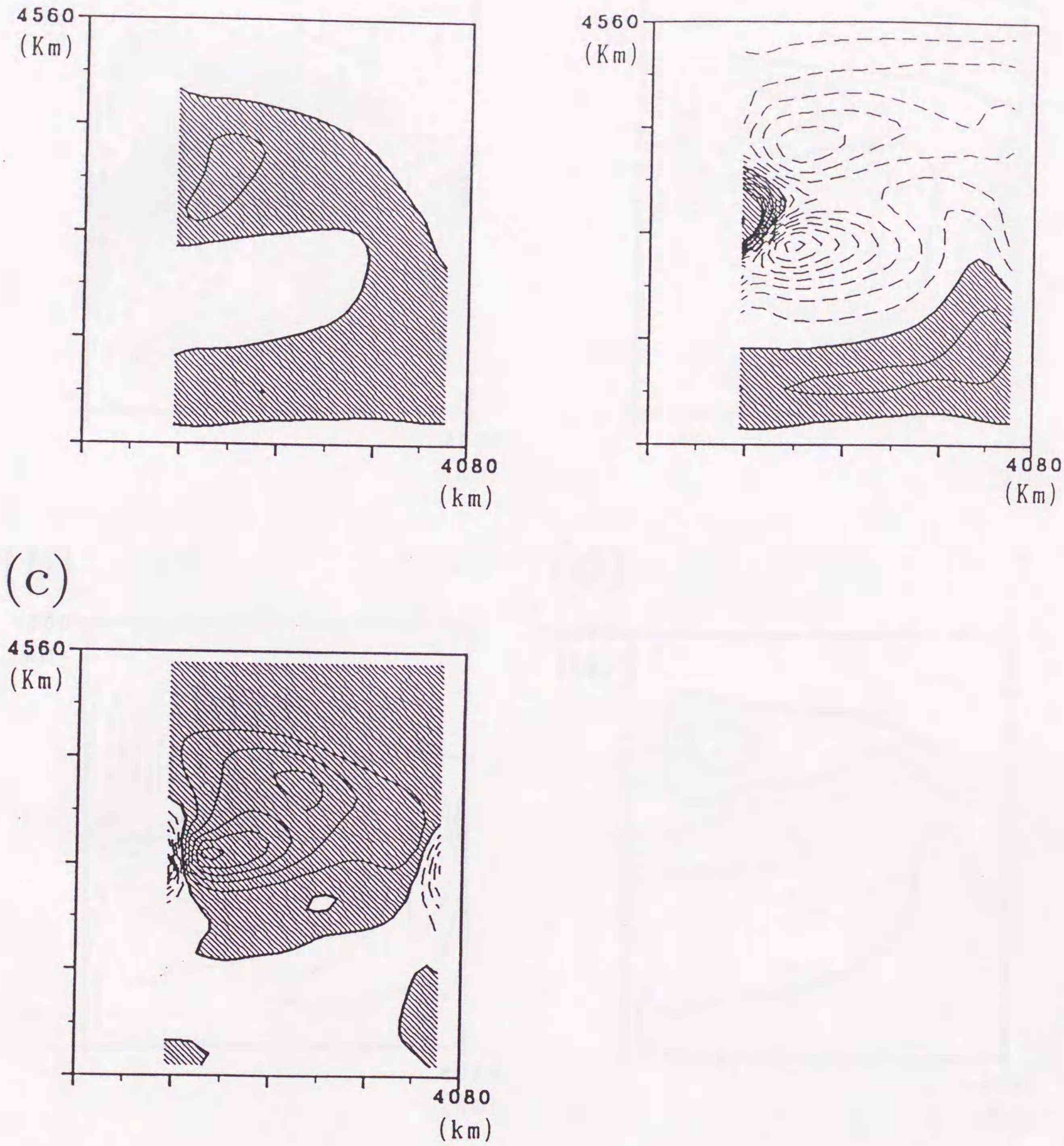


**Fig.22** Change in each component of $-(\boldsymbol{B}'\nabla)\Theta_0$ in (5.6.2) for 4-year minus 0-year. (a) $\boldsymbol{U}$, (b) $\boldsymbol{u}'$ and (c) $\lambda(H_1H_2/h)\boldsymbol{L}\{(T_1-T_2)/f\}$. Hatched area indicates positive value. Contour interval is $5\times10^{-5}$ °C cm s$^{-1}$.

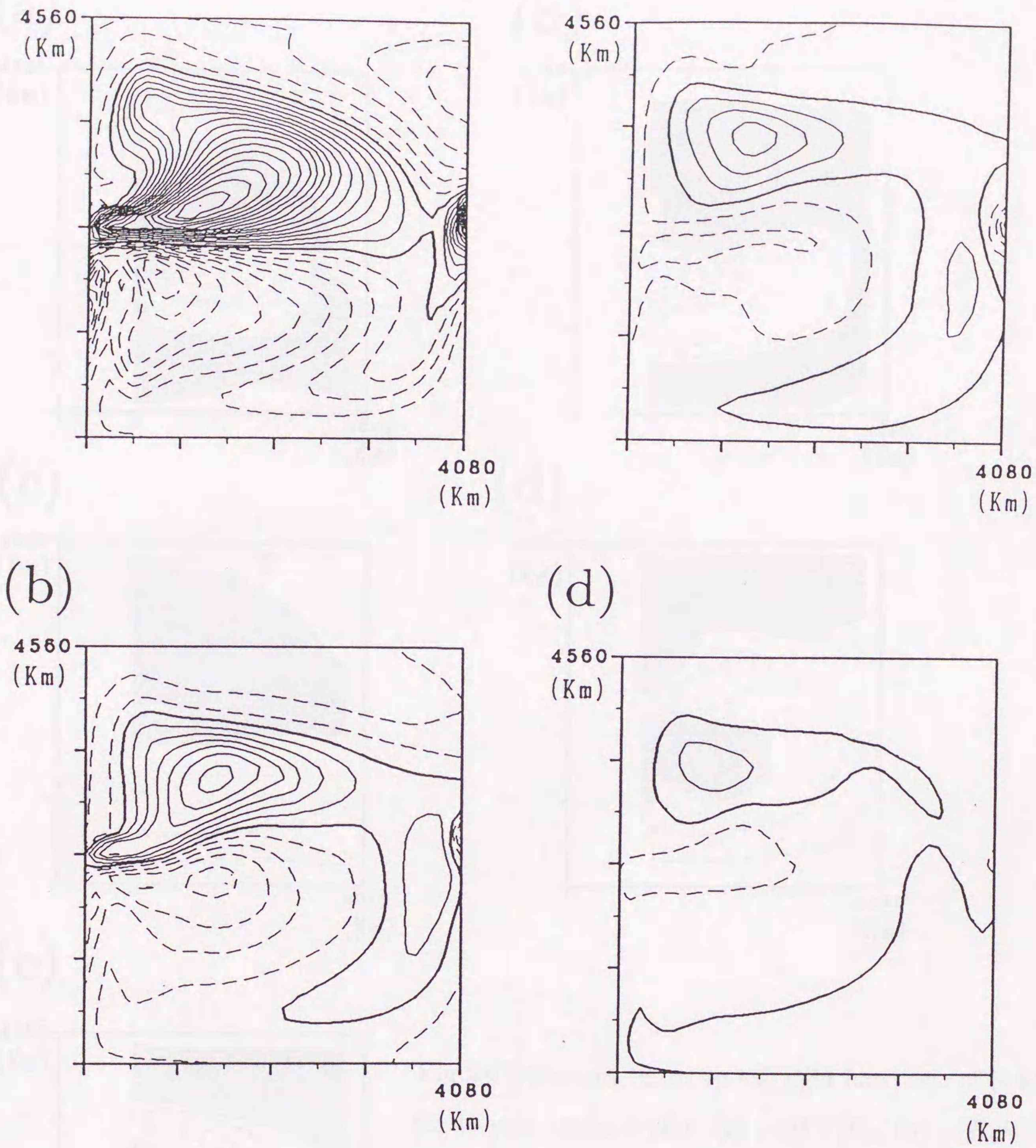


**Fig.23** Differences of $\Theta/h$ for (a) 5-yr minus 0-yr, (b) 10-yr minus 5-yr, (c) 15-yr minus 10-yr and (d) 20-yr minus 15-yr. Dashed line indicates negative value. Contour interval is 0.05°C.

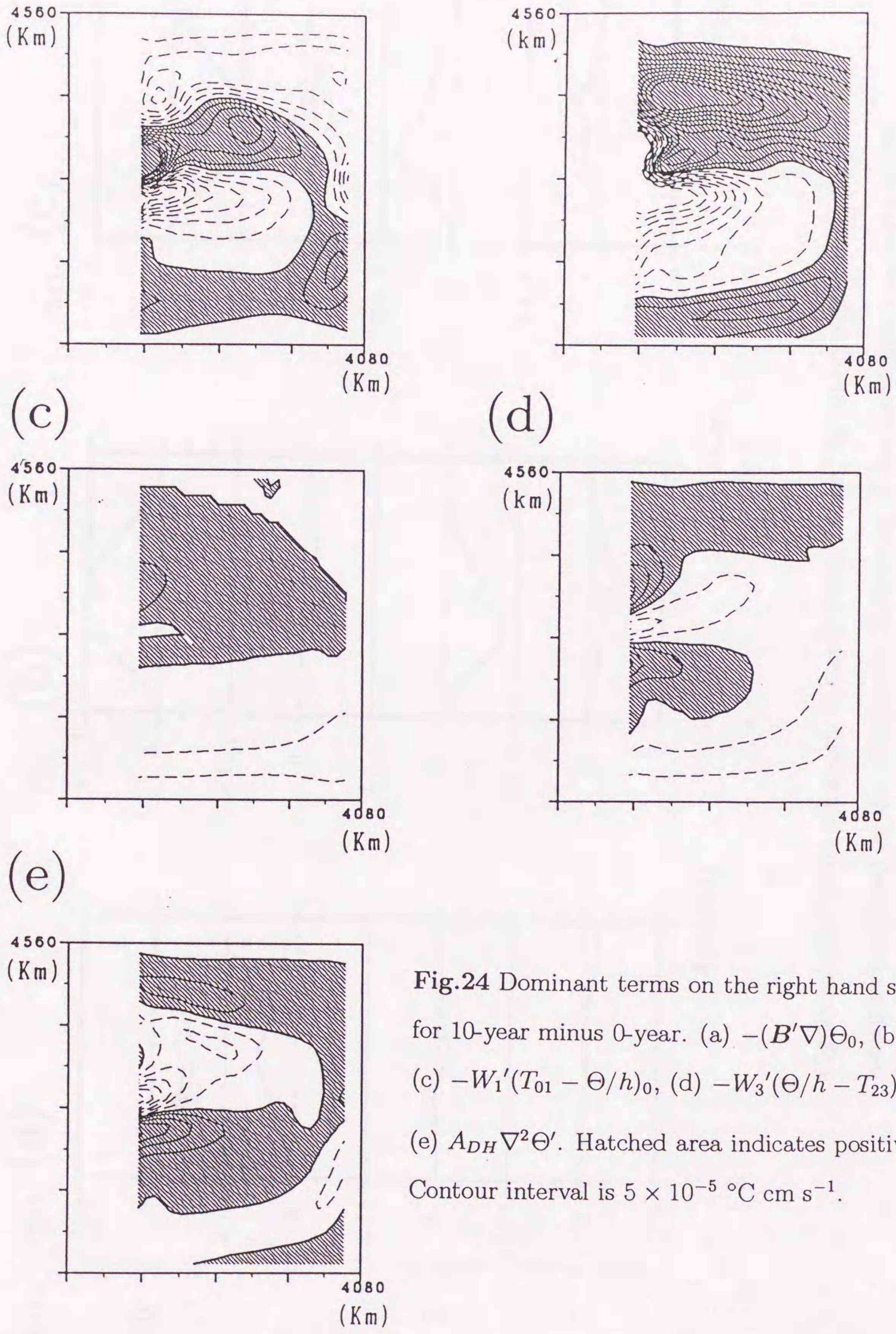


**Fig.24** Dominant terms on the right hand side of (5.6.2) for 10-year minus 0-year. (a) $-(\boldsymbol{B}'\nabla)\Theta_0$, (b) $-(\boldsymbol{B}_0\nabla)\Theta'$, (c) $-W_1'(T_{01}-\Theta/h)_0$, (d) $-W_3'(\Theta/h-T_{23})_0$ and (e) $A_{DH}\nabla^2\Theta'$. Hatched area indicates positive value. Contour interval is $5\times10^{-5}$ °C cm s$^{-1}$.

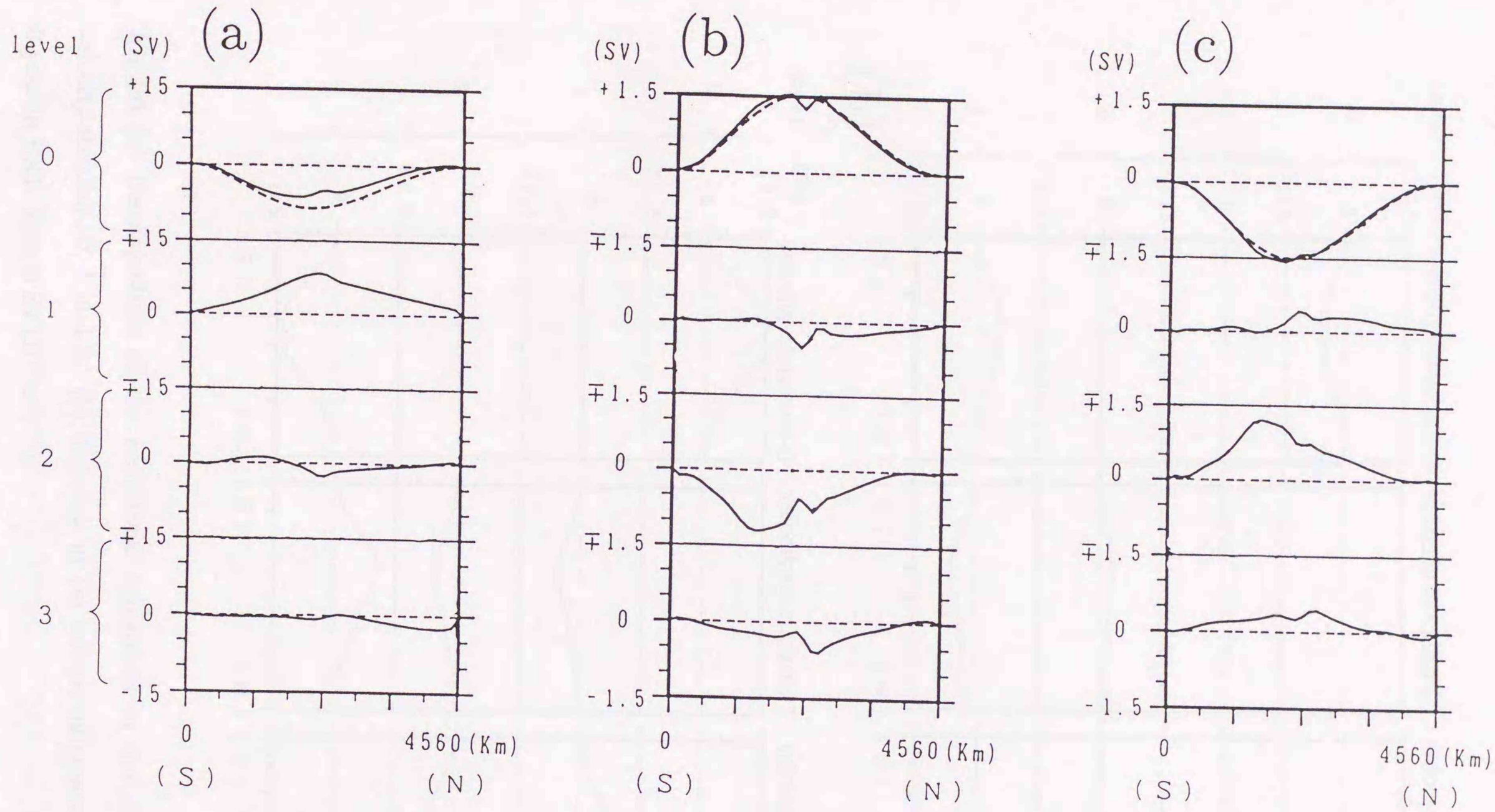


**Fig.25** (a) Meridional transports in steady state. Dashed line in (a) indicates the Ekman transport calculated by the wind stress. Differences of the meridional transports for 20-year minus 0-year in (b) EX1 and (c) EX2. Dashed lines in (b) and (c) indicate changes in the Ekman transport calculated by the wind stress change. Unit is Sv ($10^6$ $m^3s^{-1}$).

(a)

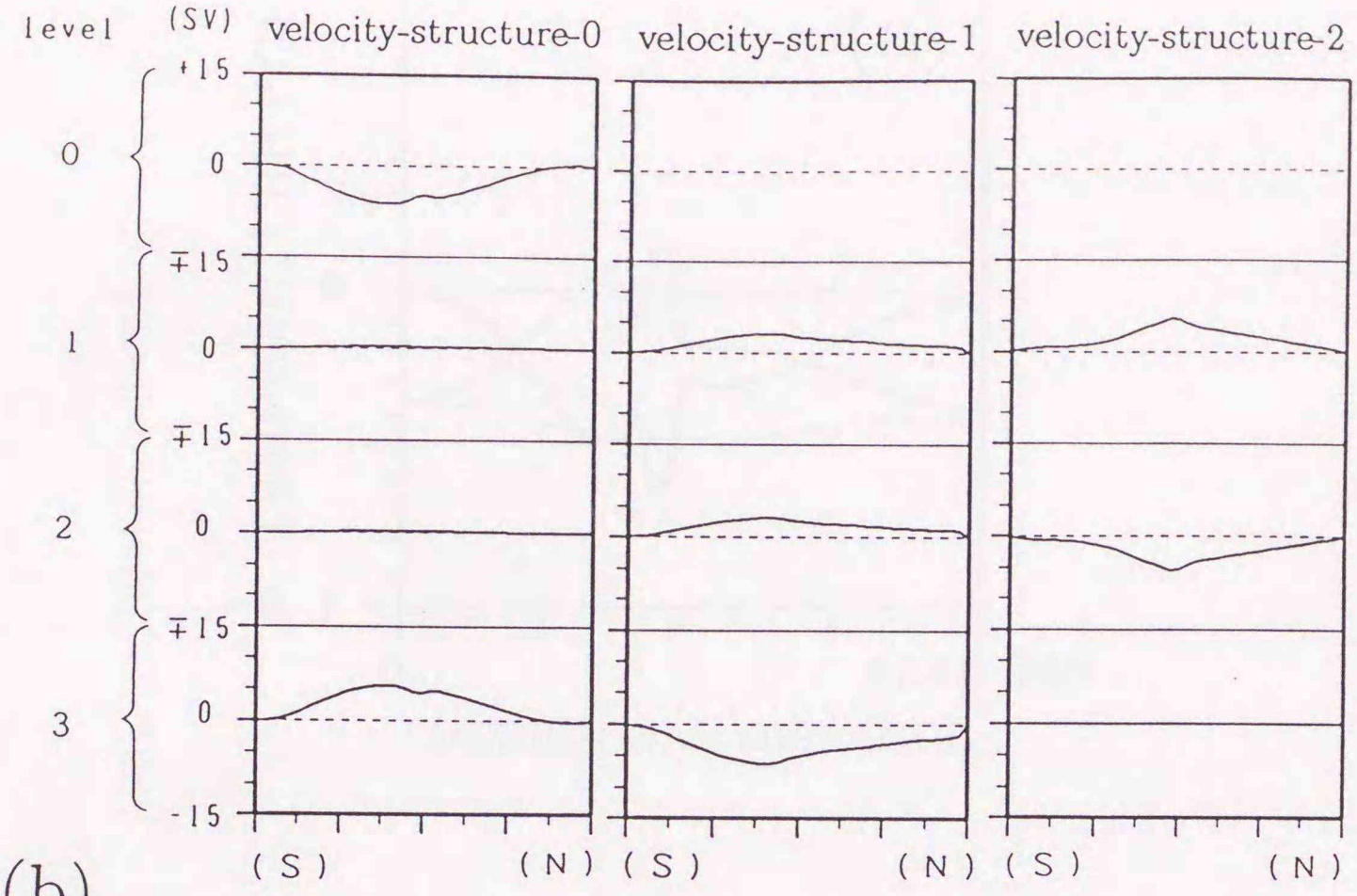


(b)

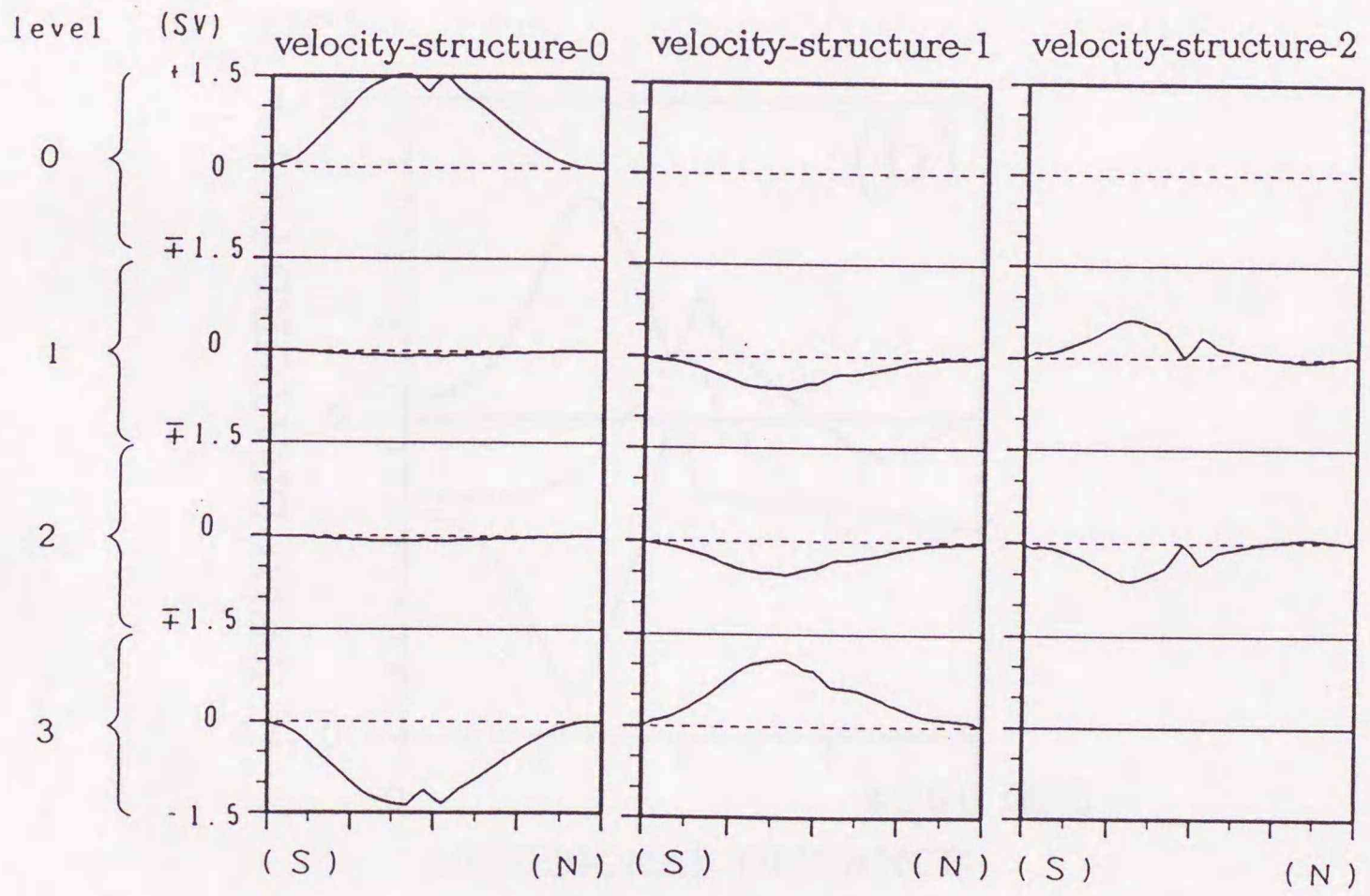


**Fig.26** (a) Decomposition of the meridional transports in the steady state into the velocity-structure-0, 1 and 2. (b) Same as in (a) except differences for 20-year minus 0-year in EX1. Unit is Sv ($10^6$ $m^3s^{-1}$).

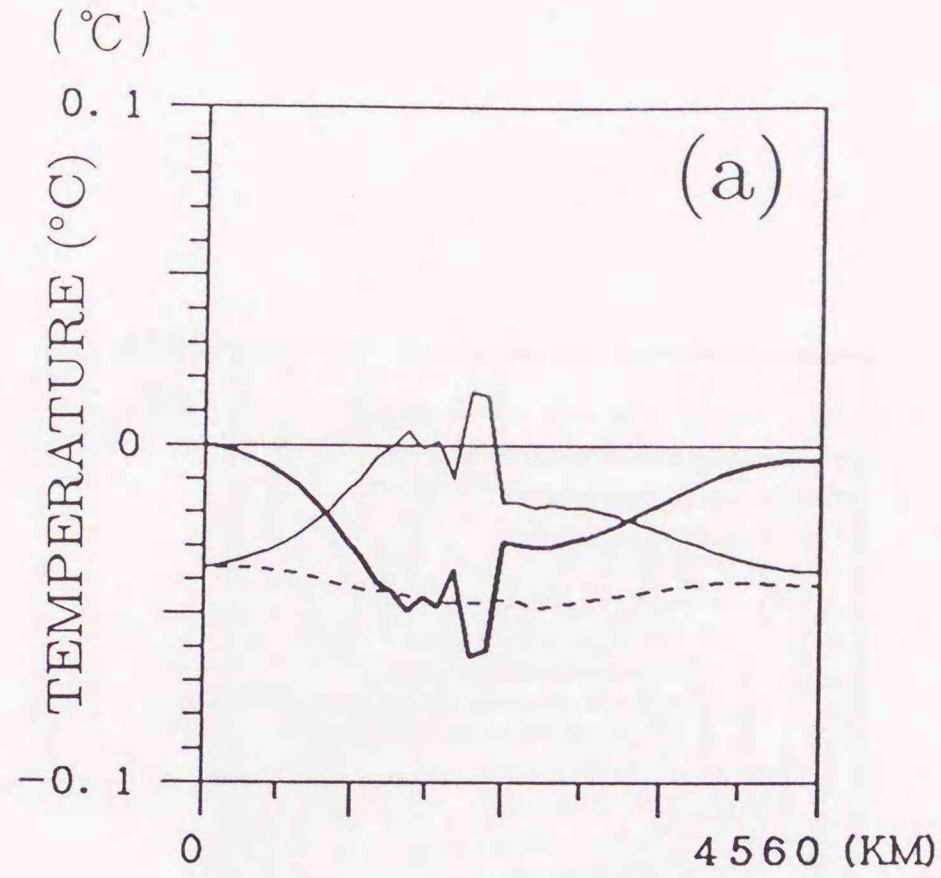


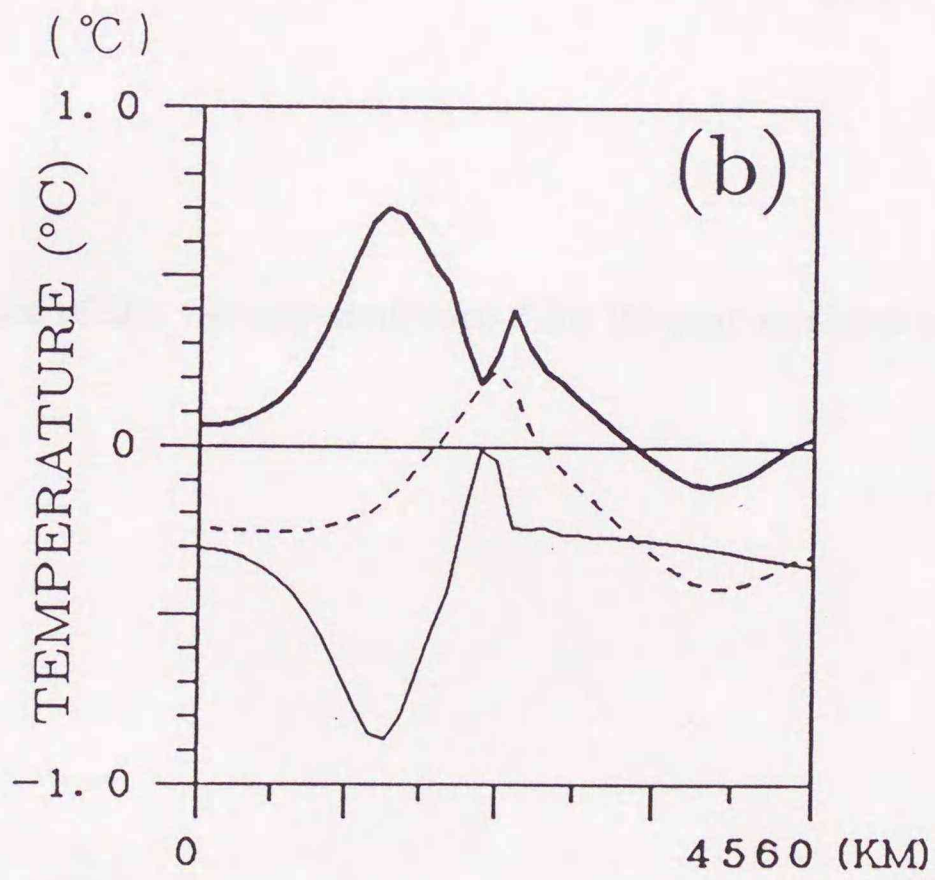


**Fig.27** (a) Difference of $\Gamma/H$ for 20-year minus 0-year in EX1. Solid line and dashed line indicate values at the western boundary and eastern boundary, respectively. Bold solid line indicates difference of values at both boundaries. (b) Same as (a) except $\Theta$.

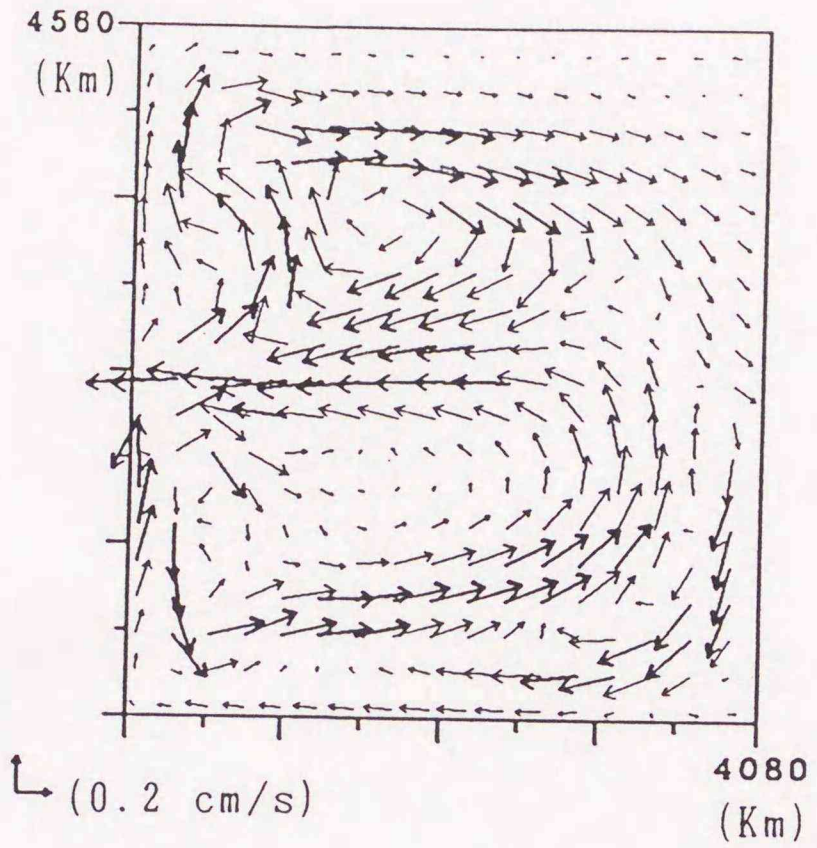


**Fig.28** Difference of the velocity-structure-2 for 20-year minus 0-year in EX1.

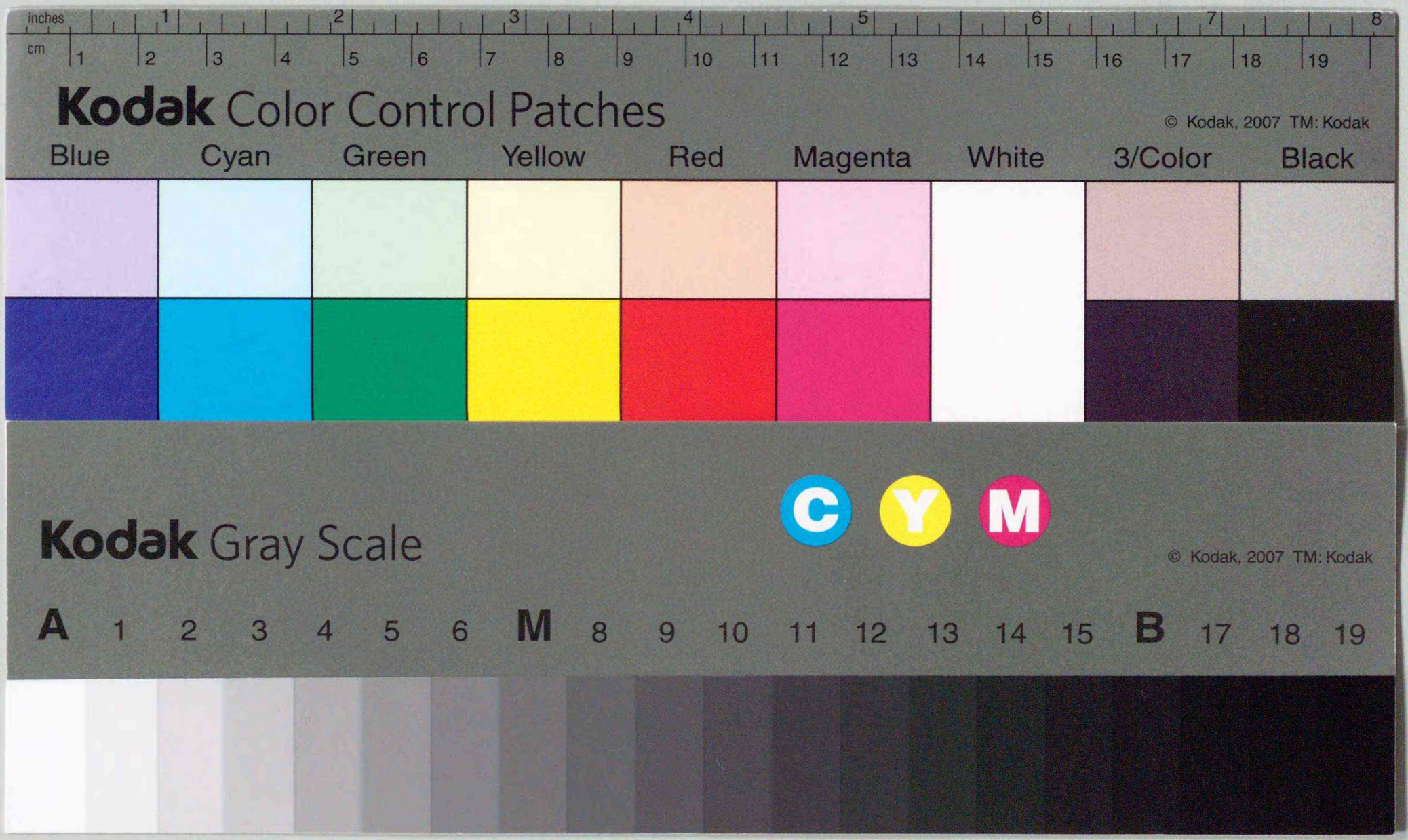
inches
cm
Kodak Color Control Patches
© Kodak, 2007 TM: Kodak
Blue
Cyan
Green
Yellow
Red
Magenta
White
3/Color
Black
Kodak Gray Scale
C
Y
M
© Kodak, 2007 TM: Kodak
A 1 2 3 4 5 6 M 8 9 10 11 12 13 14 15 B 17 18 19